



## Cloud-Top Phase Characterization of Extratropical Cyclones over the Northeast and Midwest United States: Results from IMPACTS

TROY J. ZAREMBA<sup>a,b</sup>, ROBERT M. RAUBER,<sup>a</sup> KAYLEE HEIMES,<sup>a</sup> JOHN E. YORKS,<sup>c</sup> JOSEPH A. FINLON,<sup>d,c</sup> STEPHEN D. NICHOLLS,<sup>e,c</sup> PATRICK SELMER,<sup>e,c</sup> LYNN A. MCMURDIE,<sup>f</sup> AND GREG M. MCFARQUHAR<sup>g,h</sup>

<sup>a</sup> Department of Atmospheric Sciences, University of Illinois Urbana–Champaign, Urbana, Illinois

<sup>b</sup> Department of Atmospheric and Environmental Sciences, University at Albany, State University of New York, Albany, New York

<sup>c</sup> NASA Goddard Space Flight Center, Greenbelt, Maryland

<sup>d</sup> Earth System Science Interdisciplinary Center, University of Maryland, College Park, College Park, Maryland

<sup>e</sup> Science System and Applications, Inc., Lanham, Maryland

<sup>f</sup> Department of Atmospheric Sciences, University of Washington, Seattle, Washington

<sup>g</sup> Cooperative Institute for Severe and High-Impact Weather Research and Operations, University of Oklahoma, Norman, Oklahoma

<sup>h</sup> School of Meteorology, University of Oklahoma, Norman, Oklahoma

(Manuscript received 24 July 2023, in final form 14 November 2023, accepted 5 December 2023)

**ABSTRACT:** Cloud-top phase (CTP) impacts cloud albedo and pathways for ice particle nucleation, growth, and fallout within extratropical cyclones. This study uses airborne lidar, radar, and Rapid Refresh analysis data to characterize CTP within extratropical cyclones as a function of cloud-top temperature (CTT). During the 2020, 2022, and 2023 Investigation of Microphysics and Precipitation for Atlantic Coast-Threatening Snowstorms (IMPACTS) field campaign deployments, the Earth Resources 2 (ER-2) aircraft flew 26 research flights over the northeast and midwest United States to sample the cloud tops of a variety of extratropical cyclones. A training dataset was developed to create probabilistic phase classifications based on Cloud Physics Lidar measurements of known ice and liquid clouds. These classifications were then used to quantify dominant CTP in the top 150 m of clouds sampled by the Cloud Physics Lidar in storms during IMPACTS. Case studies are presented illustrating examples of supercooled liquid water at cloud top at different CTT ranges ( $-3^{\circ} < \text{CTTs} < -35^{\circ}\text{C}$ ) within extratropical cyclones. During IMPACTS, 19.2% of clouds had supercooled liquid water present at cloud top. Supercooled liquid was the dominant phase in extratropical cyclone cloud tops when CTTs were  $> -20^{\circ}\text{C}$ . Liquid-bearing cloud tops were found at CTTs as cold as  $-37^{\circ}\text{C}$ .

**SIGNIFICANCE STATEMENT:** Identifying supercooled liquid cloud tops' frequency is crucial for understanding ice nucleation mechanisms at cloud top, cloud radiative effects, and aircraft icing. In this study, airborne lidar, radar, and model temperature data from 26 research flights during the NASA IMPACTS campaign are used to characterize extratropical cyclone cloud-top phase (CTP) as a function of cloud-top temperature (CTT). The results show that liquid was the dominant CTP present in extratropical cyclone cloud tops when CTTs were  $> -20^{\circ}\text{C}$  with decreasing supercooled liquid cloud-top frequency at temperatures  $< -20^{\circ}\text{C}$ . Nevertheless, liquid was present at CTTs as cold as  $-37^{\circ}\text{C}$ .

**KEYWORDS:** Extratropical cyclones; Cloud water/phase; Lidars/Lidar observations

### 1. Introduction

Cloud-top phase (CTP) characterization is a critical aspect of understanding cloud albedo, as well as ice particle nucleation mechanisms, growth, and fallout within extratropical cyclones. Accurate measurement and characterization of supercooled liquid water (SLW) at cloud top is essential to understanding ice

formation at cloud top through various heterogeneous ice nucleation pathways such as deposition, immersion freezing, and contact nucleation (e.g., Kanji et al. 2017; Ansmann et al. 2009; Westbrook and Illingworth 2011; de Boer et al. 2011; Field et al. 2001). Moreover, SLW indicates significant ice supersaturations across a wide temperature range at cloud top, enabling rapid diffusional growth and fallout of ice crystals if they were to form (e.g., Westbrook and Heymsfield 2011).

The dynamics of cloud-top environments within extratropical cyclones are influenced by gradients in wind shear and water vapor at cloud top. Gradients in wind shear and water vapor have the potential to destabilize the cloud-top region and induce localized vertical circulations that generate SLW.

Denotes content that is immediately available upon publication as open access.

Corresponding author: Troy Zaremba, tzaremba@albany.edu

DOI: 10.1175/JAS-D-23-0123.1

© 2024 American Meteorological Society. This published article is licensed under the terms of the default AMS reuse license. For information regarding reuse of this content and general copyright information, consult the AMS Copyright Policy ([www.ametsoc.org/PUBSReuseLicenses](http://www.ametsoc.org/PUBSReuseLicenses)).

Vertical circulations ensure that the condensate supply rate exceeds the diffusional growth rate of ice, thereby facilitating the formation of SLW at cloud top (Rauber and Tokay 1991). Convective cloud-top generating cells, for example, often develop in the presence of cloud-top potential instability driven by entrainment and cloud-top radiative cooling, and are subsequently organized by shear (Keeler et al. 2016a,b, 2017). Generating cells are highly turbulent in nature and are characterized by updrafts of  $0.75\text{--}3.00\text{ m s}^{-1}$  in the upper 1–2 km of otherwise stratiform cloud (Wexler 1955; Douglas et al. 1957; Wexler and Atlas 1959; Carbone and Bohne 1975; Rosenow et al. 2014; Kumjian et al. 2014; Henneberger et al. 2023). Qualitative and quantitative studies have reported the presence of SLW within cloud-top generating cells in various cloud systems (e.g., McFarquhar et al. 2011; Plummer et al. 2014; Wang et al. 2020; Zaremba et al. 2020). Plummer et al. (2014) analyzed data from the Profiling of Winter Storms field campaign and found SLW within 26% of generating cells observed in situ, occurring between temperatures of  $-31.4^\circ$  and  $-11.1^\circ\text{C}$ , with SLW being nearly ubiquitous at cloud top at temperatures  $> -16^\circ\text{C}$ .

Radiative cooling also plays a vital role in destabilizing cloud tops, particularly at night when longwave cooling rates are much larger without the heating caused by solar radiation. The longwave cooling process predominantly takes place at the cloud top and contributes to the creation and sustainment of cloud-top generating cells, ensuring a steady supply of SLW. Keeler et al. (2017) simulated extratropical cyclone cloud cover and revealed that the average longwave cooling rates across the domain exceeded  $0.60\text{ K h}^{-1}$ , with certain individual generating cells exhibiting cooling rates exceeding  $3.00\text{ K h}^{-1}$  during a nighttime simulation using a high-resolution mesoscale model. These cooling rates maintained instability at the cloud top, providing a sustained source of instability for generating cells to form with varying vertical velocities.

Despite its importance, relatively few studies have investigated CTP in extratropical cyclones using remote sensing data. Naud et al. (2006) used composites of clouds and environmental properties centered on storm pressure minimums to understand how *Terra* and *Aqua* Moderate Resolution Imaging Spectroradiometer (MODIS) cloud-top properties vary about extratropical cyclone pressure centers. They found a relationship between ice phase fraction and cloud-top temperature (CTT) obtained from two winters of MODIS retrievals over the North Atlantic and North Pacific. Higher glaciation rates typically occurred at higher cloud-top temperatures south and east of pressure minimums for each storm. Naud and Kahn (2015) used Atmospheric Infrared Sounder (AIRS) data to analyze CTP in Northern Hemisphere extratropical cyclones between December and February of 2006–10. They found that warm-frontal clouds are typically dominated by ice, while liquid-phase clouds often occur outside of the warm-frontal region. Supercooled or mixed-phase clouds were typically found in the southwestern quadrant of extratropical cyclones where elevated convection was most likely. Despite these studies showing potential relationships between storm thermodynamic environments at cloud top and CTP, few studies have examined and quantified CTP as a function of CTT within northeast and midwest U.S. extratropical cyclones.

Increasing interest in the dynamics and thermodynamics of cloud-top environments, CTP, and elevated convective substructures, the lack of remote sensing observations to characterize cloud-top regions, and societal impacts of recent winter storms motivated the National Aeronautics and Space Administration (NASA) Investigation of Microphysics and Precipitation for Atlantic Coast-Threatening Snowstorms field campaign (IMPACTS; McMurdie et al. 2022). The objective of this study is to quantify, using IMPACTS airborne lidar, W-band radar, and model reanalysis data, the fraction of sampled cloud tops observed over extratropical cyclone cloud systems that are dominated by SLW at cloud top as a function of CTT. A lidar phase identification scheme is developed and is used to differentiate between liquid or ice dominated cloud top.

The remaining sections of this paper are organized as follows: Section 2 provides details on the flight strategy employed during the IMPACTS campaign and describes the different types of storms sampled. Section 3 describes the data used in the analysis. Section 4 outlines the lidar phase classification algorithm, the methodology used to estimate CTTs, and compares the results obtained using the lidar phase algorithm with those from the default NASA Cloud Physics Lidar (CPL) phase algorithm. The identification of cloud top, case studies that exemplify the presence of SLW at different CTT ranges within extratropical cyclones ( $-35^\circ < \text{CTT} < 3^\circ\text{C}$ ), and the quantification of CTP is presented in section 5. Key findings of this study in relation to previous studies are discussed in section 6. Conclusions are summarized in section 7.

## 2. Sampling strategy

The IMPACTS field campaign was designed to investigate the microphysical and remote sensing properties of mesoscale snowbands in extratropical cyclones because of their significant impact on snowfall totals over the northeast and midwest United States. During the campaign there were two research aircraft: the NASA Earth Resources 2 (ER-2) which flew at high altitudes ( $\sim 20\text{ km}$ ) sampling clouds with four different radar wavelengths as well as the CPL. The NASA P-3 Orion flew in-cloud taking in situ microphysics measurements generally well below cloud top. Both aircraft primarily flew repeated flight legs orthogonal to mesoscale snowbands observed using ground-based radars, sampling the environment and microphysical characteristics within and outside of the bands. This study focuses on remote sensing data from the ER-2, specifically the CPL and the W-band Cloud Radar System (CRS). The CRS was chosen because of its higher sensitivity and greater ability to detect nonprecipitating cloud particles relative to other radars deployed on the ER-2.

Three IMPACTS deployments occurred during January and February 2020, 2022, and 2023. During that time the ER-2 sampled 26 winter storms over the midwest and northeast United States. Extratropical cyclones sampled were classified based on their low pressure tracks across/near the continental United States. Figure 1 shows representative storm types sampled using *GOES-16*  $10.35\text{ }\mu\text{m}$  brightness temperature and all ER-2 flight tracks flown to sample similar events. Table 1 summarizes storm category, research flight leg start/end times,

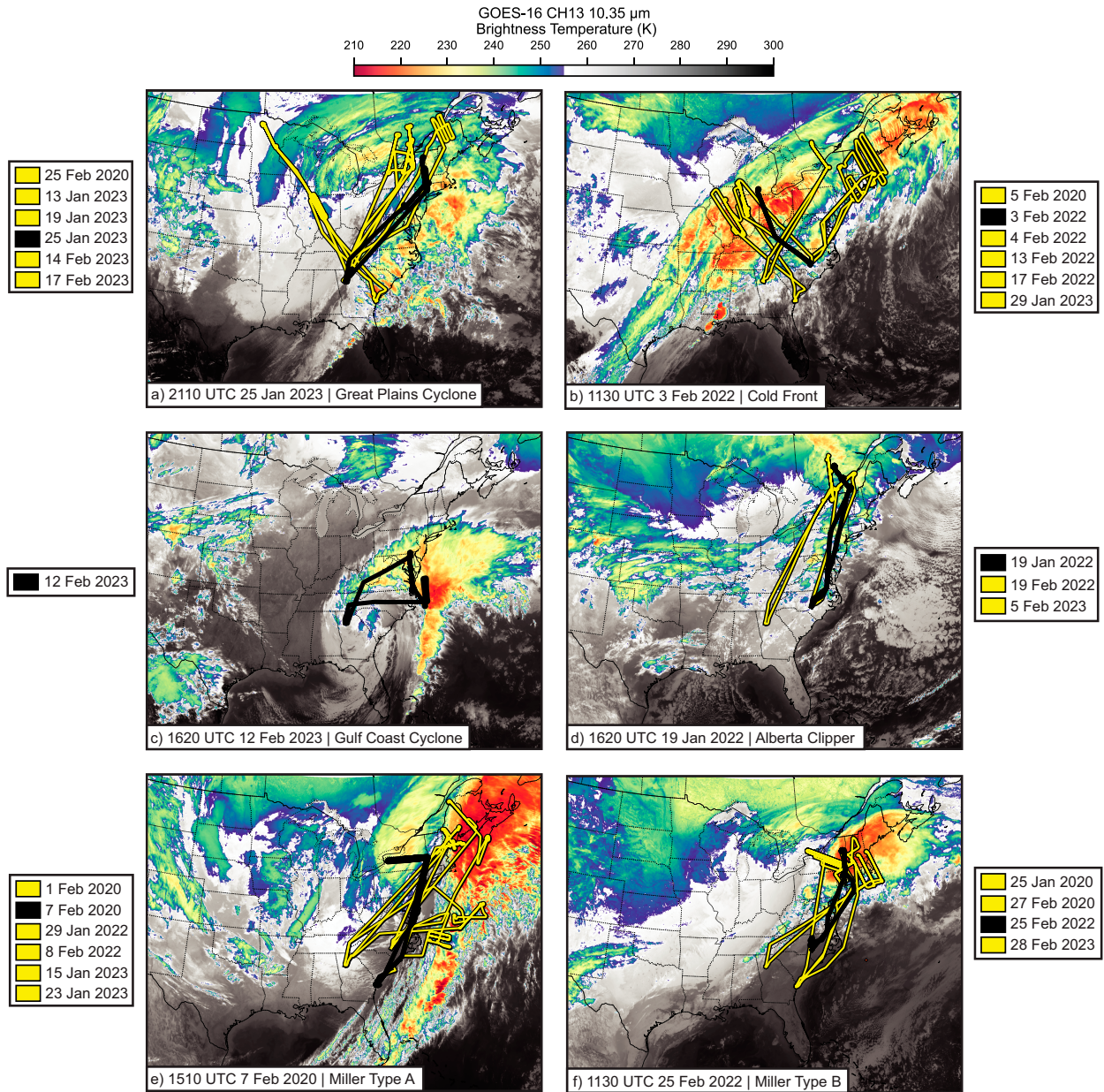


FIG. 1. The 10.35  $\mu\text{m}$  GOES-16 brightness temperature for representative extratropical cyclones observed over the northeast and midwest United States. Representative storm systems included (a) Great Plains cyclone, (b) cold front, (c) low originating over the Gulf Coast, (d) Alberta clipper, (e) Miller type-A cyclone, and (f) Miller type-B cyclone. Black flight tracks correspond to the representative storm's satellite image shown. Yellow flight tracks correspond to flights that sampled similar storms of the same category over the northeast and midwest United States.

number of flight legs flown on a given research flight, and the cumulative distance traveled along the research flight legs by the ER-2 (excluding the ferry legs). The category was decided based on the region of cyclogenesis, how the low pressure center evolved with time, and if there was secondary cyclogenesis along the East Coast before being sampled by IMPACTS.

Cyclones moving northeastward along the U.S. East Coast and intensifying were classified as Miller type-A, Miller type-B, or Great Plains cyclones, depending on their point of origin. Six Great Plains cyclones were sampled by the ER-2 during the

three deployments. These lows typically formed over the upper Midwest and Great Plains before moving northeast along/near the Canadian border and exhibited no redevelopment along the East Coast. Four flights sampled the clouds in these cyclones over the northeast United States, one over Illinois, and one over the upper Great Plains (Fig. 1a). These were typically deeper cloud systems (cloud depth > 8 km), with rain to the south and snow to the north. Six Arctic cold fronts were sampled where the ER-2 flew consecutive flight legs across the fronts. These fronts had no strong low pressure center, but

TABLE 1. Flight leg start and end times, number of flight legs flown, and total distance traveled along the legs by the ER-2.

Deployment	Flight leg start time	Flight leg end time	Number of flight legs	Cumulative flight leg length (km)
<b>Great Plains cyclones</b>				
2020	2145 UTC 25 Feb	0142 UTC 26 Feb	11	2146
2023	0550 UTC 13 Jan	0909 UTC 13 Jan	7	1692
2023	2140 UTC 19 Jan	0147 UTC 19 Jan	8	1622
2023	1902 UTC 25 Jan	2326 UTC 25 Jan	9	1986
2023	0018 UTC 15 Feb	0246 UTC 15 Feb	6	1025
2023	1448 UTC 17 Feb	1645 UTC 17 Feb	6	922
<b>Cold fronts</b>				
2020	1355 UTC 5 Feb	0001 UTC 6 Feb	7	1554
2022	1443 UTC 3 Feb	1604 UTC 3 Feb	2	433
2022	1444 UTC 4 Feb	1911 UTC 4 Feb	6	2028
2022	1212 UTC 13 Feb	1523 UTC 13 Feb	6	1310
2022	1736 UTC 17 Feb	2233 UTC 17 Feb	11	2137
2023	1455 UTC 29 Jan	1640 UTC 29 Jan	4	746
<b>Gulf Coast cyclone</b>				
2023	1440 UTC 12 Feb	1918 UTC 12 Feb	9	1887
<b>Alberta clippers</b>				
2022	1231 UTC 19 Jan	1628 UTC 19 Jan	11	1265
2022	1258 UTC 19 Feb	1556 UTC 19 Feb	6	1073
2023	1516 UTC 5 Feb	1811 UTC 5 Feb	6	1435
<b>Miller type-A cyclones</b>				
2020	1222 UTC 1 Feb	1408 UTC 1 Feb	5	795
2020	2145 UTC 7 Feb	1613 UTC 7 Feb	6	1238
2022	0035 UTC 30 Jan	0156 UTC 30 Jan	7	487
2022	1253 UTC 8 Feb	1814 UTC 8 Feb	7	2166
2023	1500 UTC 15 Jan	1811 UTC 15 Jan	7	1200
2023	1425 UTC 23 Jan	1709 UTC 23 Jan	8	1091
<b>Miller type-B cyclones</b>				
2020	2000 UTC 25 Jan	2300 UTC 25 Jan	11	1604
2020	0915 UTC 27 Feb	1304 UTC 27 Feb	9	2324
2022	0923 UTC 25 Feb	1325 UTC 25 Feb	10	1696
2023	1102 UTC 28 Feb	1403 UTC 28 Feb	6	1235

rather a series of weak low pressure systems that propagated along the strong temperature gradient. The temperature gradient typically formed and was reinforced by a strong Canadian high pressure system bringing anomalously cold air southward. Widespread precipitation, both rain and snow, was typically found on the cold side of the front (Fig. 1b). One Gulf Coast low was sampled by the ER-2 that formed off the northwest coast of Florida, traversed over the southeast United States, and then up the East Coast with no redevelopment (Fig. 1c). Three Alberta clippers were sampled by the ER-2 over southeastern Canada during the three deployments. These were typically associated with weaker low pressure systems originating over western Canada and traversing the U.S.–Canadian border (Fig. 1d). Six Miller type-A and five Miller type-B storms (Miller 1946) were also sampled by the ER-2 during IMPACTS. Miller type-A cyclones develop along a cold front located along the East Coast of the United States. Miller type-B cyclones develop along the East Coast of the United States but to the southeast of an older

cyclone on the western side of the Appalachian Mountains (Figs. 1e,f).

The flight paths of the ER-2 were composited with respect to the tracked paths of the centers of observed cyclones. Each cyclone's pressure minimum was found using fifth-generation European Centre for Medium-Range Weather Forecasts reanalysis (ERA5; Hersbach et al. 2020) mean sea level pressure. This minimum was tracked over time, with positions interpolated between reanalysis output. The proximity of the ER-2's flight paths to the cyclone's surface low pressure center was estimated every second (Fig. 2). Typically, the ER-2 was sampling within the northwest quadrant of IMPACTS storms. This compositing procedure could not be applied for flights across extensive Arctic cold fronts. Figure 3 shows an example of an Arctic cold front sampled on 3 February 2022 by the ER-2 with strong high pressure system bringing anomalously cold air southward. During Arctic-frontal events, the ER-2 predominantly sampled cloud cover 10–400 km behind the surface front.

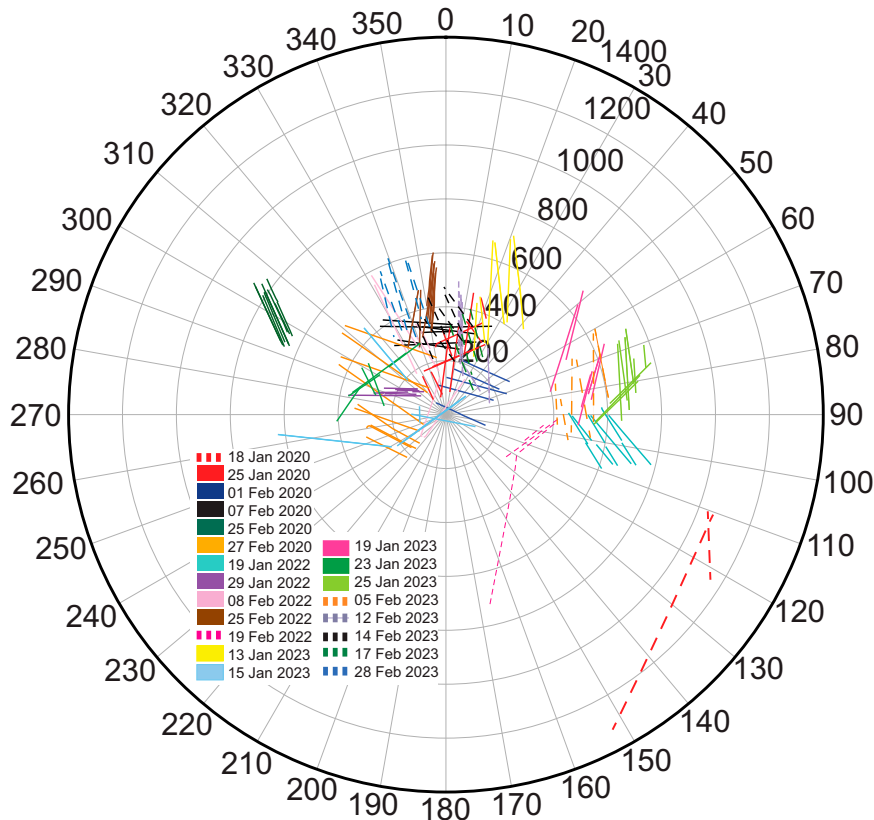


FIG. 2. ER-2 flight tracks in low relative coordinates. Distances are shown in kilometers away from the cyclone's pressure minimum.

### 3. Data

#### a. CPL

The CPL (McGill et al. 2002) is a backscatter lidar designed to operate simultaneously at two visible and one infrared wavelength (355, 532, and 1064 nm) and provide multiwavelength lidar measurements at high spatial and temporal resolution. The CPL has a vertical resolution of 30 m and a horizontal resolution that varied due to the speed of the ER-2 but during IMPACTS was typically 200 m. The CPL was nominally pointed at  $2^\circ$  toward the nose of the ER-2 which typically had a pitch of  $1^\circ$  for a total  $3^\circ$  offset allowing CPL returns to avoid specular reflection from horizontally oriented ice crystals. For a cloud located 10 km from the CPL, the receiver footprint is only  $\sim 1$  m (Yorks et al. 2011a). The CPL provided observations of the backscatter coefficient ( $\beta$ ) and depolarization ratio ( $\delta$ ), which are used herein at 1064 nm to determine CTP. The CPL measures the total backscatter ( $\beta$ ) signal (particle plus molecular) and cross-polarized backscatter signal to estimate  $\delta$  of the return signal from cloud and aerosol particles. The quantity  $\beta$  is a measure of how strongly the volume sampled scatters light back to the lidar at a  $180^\circ$  scattering angle. The quantity  $\delta$  measures the degree to which particles in a scattering volume modify the polarization state of incident light, which is related to the sphericity of the

particles in the scattering volume (Noel et al. 2004; Yorks et al. 2011b). In this paper, these two lidar parameters ( $\beta$  and  $\delta$ ) are used to discriminate between liquid and ice. Figures 4a–c are a sample of the radar and lidar data observed on 7 February 2020, including an example of  $\beta$  and  $\delta$  in Figs. 4d and 4e.

The CPL level 2 data products consisted of vertical atmospheric profiles with an along-track horizontal resolution of 800 m to 1.2 km, depending on the aircraft ground speed. Each profile contained vertical bins with 30 m vertical resolution, hereafter referred to as *elements*. When the ER-2 was flying at approximately 20 km, a vertical column contained  $\sim 667$  elements. This study is limited to phase retrievals at cloud top because optically thick cloud cover fully attenuated the CPL signal beneath cloud top. The optical depths of liquid cloud tops are influenced by cloud thickness, water content, and droplet size, and generally causes lidar signals to attenuate quickly when the optical depth nears 3 (Venema et al. 2000). The CPL signal in some instances during IMPACTS penetrated several kilometers beneath cloud top. These cases often were associated with optically thin ice clouds like cirrus.

#### b. CRS

The CRS is a W-band (94 GHz) radar that flies in nadir pointing mode on the NASA ER-2 providing observations of equivalent reflectivity factor,  $Z_e$ , and Doppler radial velocity,

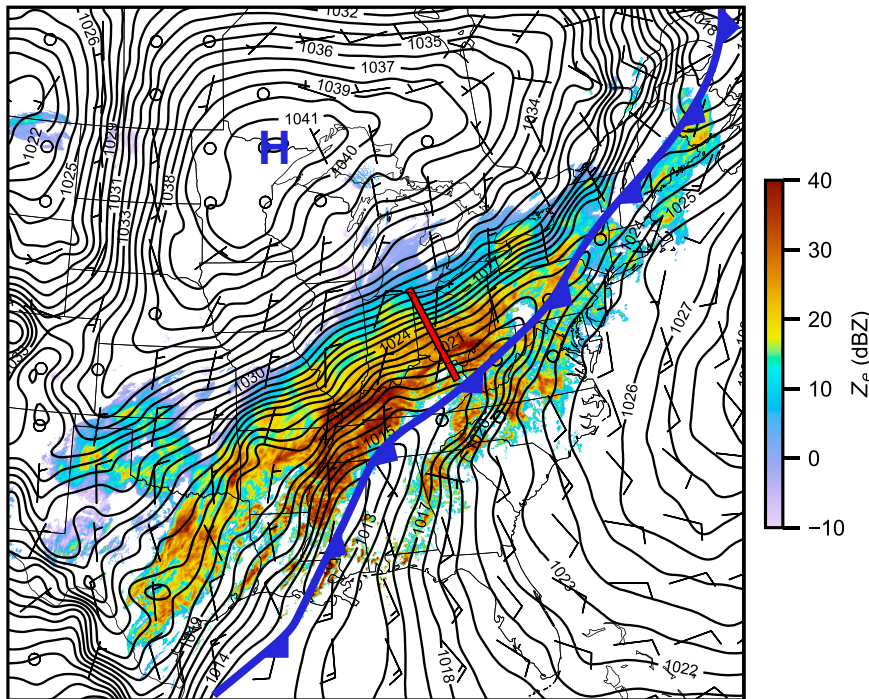


FIG. 3. Multi-Radar Multi-Sensor (MRMS; Zhang et al. 2016) radar reflectivity overlaid with RAP analysis mean sea level pressure (contoured) and 10 m wind barbs valid at 1600 UTC 3 Feb 2022. Wind barb convention on all panels: half barb =  $5 \text{ m s}^{-1}$  and full barb =  $10 \text{ m s}^{-1}$ . The red line was the science flight track flown between 1442 and 1604 UTC 3 Feb 2022.

$V_r$ . This analysis examines the horizontal variability of cloud substructures and circulations using the CRS fixed nadir beam and takes advantage of higher resolution  $V_r$  measurements due to its smaller beamwidth, reduced nonuniform beam filling, and higher sensitivity relative to other radars deployed on the ER-2 (McLinden et al. 2021a,b). The CRS beamwidth is  $0.468^\circ$  with a footprint of 0.16 km at the surface when the aircraft is flying at 20 km altitude. Figures 4a and 4b show  $Z_e$  and  $V_r$  along a flight track on 7 February 2020.

The CPL has a much smaller wavelength than the CRS, which makes it comparatively more sensitive to smaller particles present at cloud top. Therefore, the CPL often detected cloud well above radar cloud-top echo (typically 250 m to 2 km above). Section 4b includes further analysis of radar characteristics, specifically examining the storm structure along the flight legs in relation to the characterization of CTP.

#### c. RAP analysis data

CTT was estimated using data obtained from hourly 13-km Rapid Refresh (RAP; Benjamin et al. 2016) analysis data. The nearest RAP grid point in time and space was used to estimate CTT for a given cloud-containing profile. CTT was linearly interpolated between two model pressure levels nearest in height to each CPL measured cloud-top height to estimate CTT. This method was used to estimate CTT for each lidar profile along every research flight leg during IMPACTS. The RAP analysis data were used rather than the High

Resolution Rapid Refresh (HRRR) analysis because it was also available during the 2015 Radar Definition Experiment (RADEX; Tridon et al. 2019; Houze et al. 2017) field campaign. The RADEX data were used to develop the training dataset for liquid clouds (see section 4b). Using the RAP analysis data allowed us to maintain a consistent analysis dataset during the building of the liquid and ice training datasets, and the subsequent statistical analysis of the IMPACTS data.

#### d. UIUC rawinsonde data

During the 2020, 2022, and 2023 field campaigns, the University of Illinois Urbana–Champaign (UIUC) launched 83 iMet-4 rawinsondes from various locations across the Northeast, primarily along the flight tracks of the ER-2 and P-3 aircraft. These rawinsondes were used herein to establish the accuracy of temperature measurements using the RAP analysis. The manufacturer-stated accuracy of UIUC rawinsondes was  $\pm 0.2^\circ\text{C}$  for temperature. To facilitate direct comparisons between the RAP analysis and observed temperatures, the rawinsonde and RAP analysis data were interpolated to 25 m height intervals. Of the 83 rawinsondes, 8 were terminated before reaching cloud top, and were therefore not used in this analysis. Temperature measurements from the remaining 75 rawinsondes were matched to the RAP analysis data interpolated to the sonde's latitude, longitude, altitude, and time.

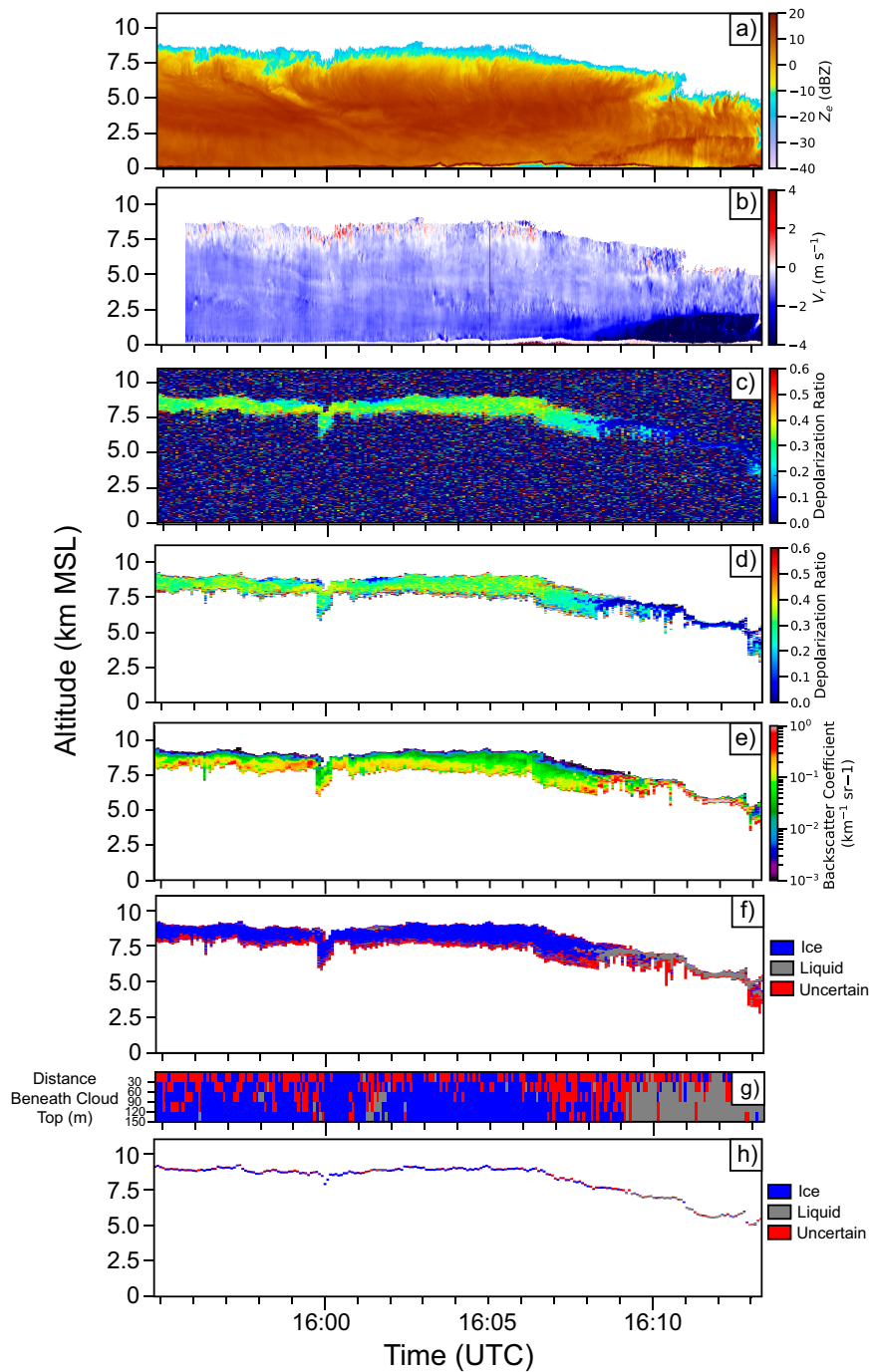


FIG. 4. An example from 1540:50 to 1613:18 UTC 7 Feb 2020 showing the processing of the flight leg to classify CTP. Time is in UTC and height is in kilometers above MSL. (a) CRS  $Z_e$ , (b) CRS  $V_r$ , (c) CPL 1064 nm depolarization ratio (all data), (d) CPL 1064 nm depolarization ratio ( $\delta$ ) after the NASA cloud mask was applied, (e) CPL 1064 nm backscatter coefficient ( $\beta$ ) after the NASA cloud mask was applied, (f) phase classification for every element along the flight leg (ice is blue, gray is liquid, and red is uncertain), and (g) CTP classification (top 150 m, first five bins). Each bin represents 30 m. This corresponds to the first five elements identified as cloud top in (h). (h) CTP (top 150 m).

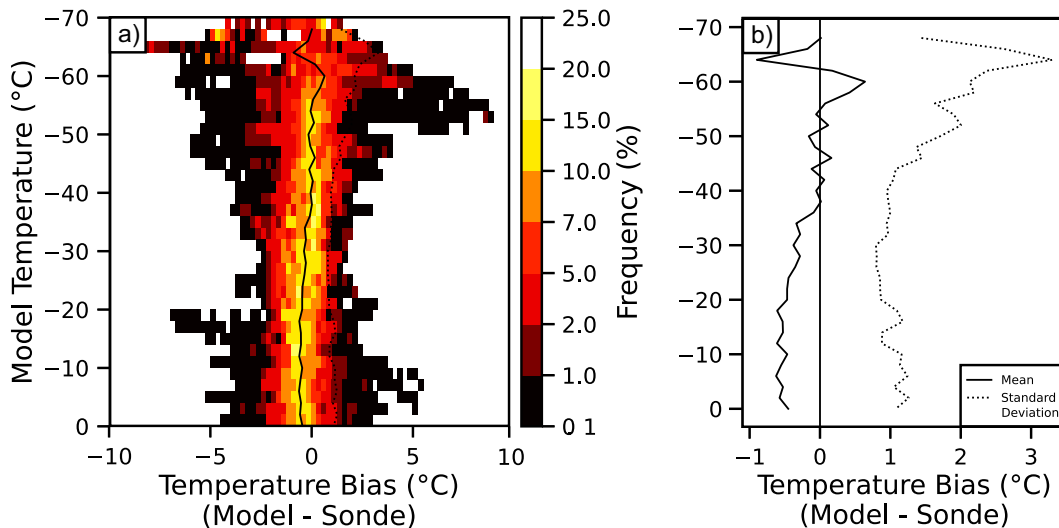


FIG. 5. (a) Discrepancies between RAP analysis temperatures and rawinsonde observations, matched by location and time, represented by a contoured frequency of RAP temperature bias as a function of RAP analysis temperatures. The solid black line represents the mean difference between the RAP analysis and rawinsonde temperatures and the dotted line represents the standard deviation. (b) An enlarged view of (a), showing the mean and standard deviation of the temperature bias.

#### e. Comparison of RAP analysis and UIUC rawinsonde temperatures

Figures 5a and 5b illustrate the differences between the RAP analysis and observed temperatures as a function of the RAP analysis temperature. In the temperature range of  $-20^{\circ}$  to  $-40^{\circ}\text{C}$ , the RAP analysis mean deviation from the observed temperatures varied from  $-0.65^{\circ}\text{C}$  at  $-20^{\circ}\text{C}$  to  $0.01^{\circ}\text{C}$  at  $-40^{\circ}\text{C}$  (Fig. 5). The standard deviation of the difference was approximately  $1^{\circ}\text{C}$  for model temperatures between  $-20^{\circ}$  and  $-40^{\circ}\text{C}$ , increasing slightly above  $1^{\circ}\text{C}$  for temperatures greater than  $-20^{\circ}\text{C}$  due to discrepancies in the elevation of the low-level frontal inversions in the storms. At temperatures  $< -40^{\circ}\text{C}$ , the standard deviation increased with decreasing temperature to values of  $2^{\circ}\text{C}$  at  $-50^{\circ}\text{C}$ , and  $3^{\circ}\text{C}$  at  $-64^{\circ}\text{C}$ . The minor discrepancies between the RAP analysis and the rawinsonde temperature data between  $0^{\circ}$  and  $-40^{\circ}\text{C}$  provide confidence that the RAP analysis can be used to estimate cloud-top temperatures.

#### 4. Cloud-top phase identification

Yorks et al. (2011b) details the standard algorithm to identify cloud phase in clouds sampled by the CPL. This algorithm uses simple threshold values of model-estimated temperature measurements and the 1064 nm layer-integrated linear depolarization ratio. In the standard algorithm, if the lidar-detected mid-cloud-layer temperature within a profile was  $< -20^{\circ}\text{C}$ , the lidar-detected mid-cloud-layer altitude was  $> 8$  km, and the layer integrated volume depolarization ratio was  $> 0.27$ , then the cloud was classified as ice. If the lidar-detected mid-cloud-layer temperature was  $> -20^{\circ}\text{C}$ , the lidar-detected mid-cloud-layer altitude was  $< 8$  km, and the profile integrated depolarization ratio was  $< 0.16$ , then the cloud was classified as liquid. Otherwise, it was classified as uncertain.

SLW has frequently been observed at cloud top at temperatures  $< -20^{\circ}\text{C}$  and even at temperatures as cold as  $-31.4^{\circ}\text{C}$  in Northern Hemisphere midlatitude cyclones (e.g., Plummer et al. 2014). The analysis below therefore modifies the standard CPL cloud phase identification methodology to detect SLW at colder temperatures by incorporating backscatter coefficient and depolarization ratio measurements using probabilistic phase classification based on training datasets of known liquid and ice populations, rather than using hard threshold values of temperature and the depolarization ratio.

CTP characterization herein is based on analysis of  $\delta$  and  $\beta$  in profile elements within 150 m of cloud top. The methodology resembles the approach of past ground-based and spaceborne lidar analyses that use two-dimensional histograms to classify cloud phase (e.g., Hu 2007; Hu et al. 2009; Thorsen et al. 2015; Silber et al. 2018; Zaremba et al. 2020). In these studies, cloud phase was classified along an entire lidar or satellite time series dependent upon where data fell on a two-dimensional  $\delta$  versus  $\beta$  histogram. Several studies set arbitrary fixed boundaries between different regions of the two-dimensional histogram to discriminate cloud phase (e.g., Shupe 2007; Luke et al. 2010). Zaremba et al. (2020) developed methodology that could be used to identify CTP probabilistically based on training datasets within and over Southern Ocean clouds using a comparison of lidar backscatter coefficient and depolarization ratio. A similar methodology is used in this study to characterize extratropical cyclone CTP. This work builds training datasets for known liquid and ice populations and uses the training datasets to classify CTP for all lidar-detected cloud tops during IMPACTS. Figure 6 summarizes the processing steps explained in this section that are used to develop the phase classification algorithm.

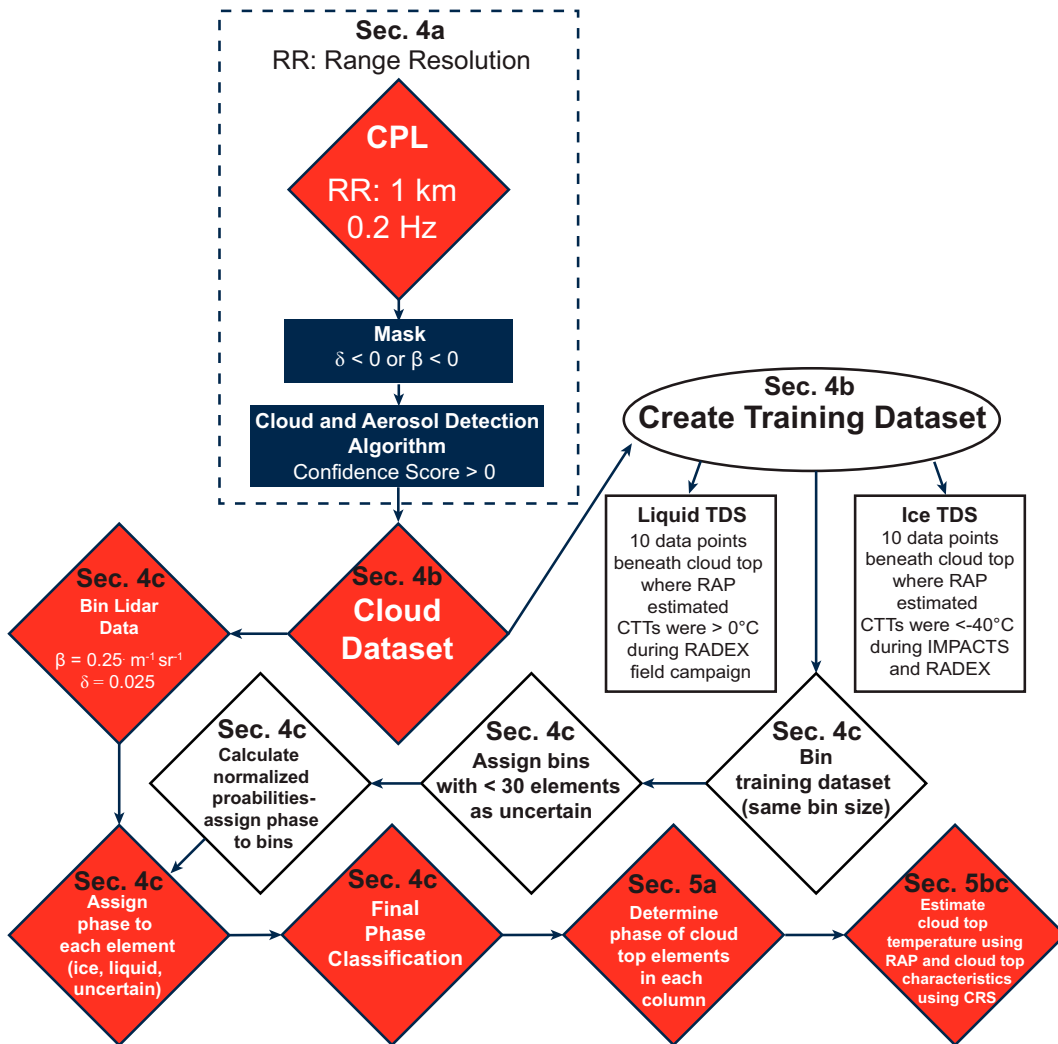


FIG. 6. Flowchart summarizing the phase identification algorithm. Processing steps taken by NASA are denoted by the dashed box. Algorithm sections in the text are noted.

*a. Cloud–aerosol discrimination algorithm*

A cloud–aerosol discrimination algorithm, based on the operational algorithms employed for NASA’s *Cloud–Aerosol Lidar and Infrared Pathfinder Satellite Observations (CALIPSO)* mission (Liu et al. 2009) and Cloud-Aerosol Transport System (CATS) lidar instrument (Yorks et al. 2021), was used to separate cloud from aerosol and clear air. First, if an atmospheric layer had a layer-integrated attenuated backscatter at 1064 nm greater than  $0.03 \text{ sr}^{-1}$  or a color ratio (1064 nm/532 nm backscatter coefficient) greater than 1, the layer was classified as high confidence cloud (CAD = 10). CAD is the cloud–aerosol detection score that ranges from –10 to 10. A value of 10 indicates complete confidence that the layer is a cloud while a layer with a CAD score equal to –10 indicates accurate classification of an aerosol layer. If the layer did not meet either of these criteria but had a 1064 nm layer integrated depolarization ratio  $> 0.27$  and midlayer temperature  $< -20^\circ\text{C}$  it was classified as high

confidence cloud (CAD = 10). For layers that did not meet both criteria, a multidimensional probability density function (PDF) technique based on the *CALIPSO* algorithm (Liu et al. 2009) was used to assign CAD scores. The PDFs were developed based on CPL measurements obtained during 11 field campaigns. Multidimensional PDFs included additional attributes such as layer altitudes and thickness, 532 nm attenuated backscatter, 1064 nm depolarization, and attenuated backscatter color ratio (1064/532 nm). Adding more attributes, or dimensions, to the PDFs resulted in smaller overlap and better skill in classifying clouds and aerosols (Liu et al. 2004). The cloud aerosol discrimination algorithm PDF analysis provides a score which is an integer value ranging from –10 to 10 for each atmospheric layer. The sign of the CAD score identifies a layer as either cloud (positive) or aerosol (negative) while the magnitude represents classification confidence. If the CAD score equaled 0, the layer is equally likely to be a cloud layer or aerosol layer, and was classified as undetermined. In this study, the first element in a

column with a CAD score  $> 0$ , classified as cloud, was determined as cloud top. Only elements that were classified as cloud by the NASA CPL cloud–aerosol detection algorithm were included in the training datasets and used to classify CTP for the IMPACTS dataset.

### b. Training dataset creation

Figure 7 shows the two-dimensional histogram ( $\delta$  versus  $\beta$ ) for all flight legs during the 2020, 2022, and 2023 IMPACTS deployments regardless of aerosol presence, cloud presence, or depth beneath cloud top. Figure 7 includes cloud elements that could be liquid, ice, or mixed phase, and elements affected by single or multiple scattering. The bin width in Fig. 7 was 0.005 for  $\delta$  and  $0.05 \text{ m}^{-1} \text{ sr}^{-1}$  for  $\beta$ . The histogram has two clusters where specific populations (cloud dominated by liquid and cloud dominated by ice) are likely concentrated based on past lidar studies (e.g., Silber et al. 2018; Zaremba et al. 2020) that examined cloud cover and subsequent phase at visible wavelengths.

IMPACTS was solely focused on sampling subfreezing cloud cover associated with extratropical cyclones and did not sample many cloud tops that were  $>0^\circ\text{C}$  that had pure liquid cloud tops. To address warmer, liquid clouds, CPL data from 15 flights during the 2015 RADEX campaign were used to help build both the ice and liquid training datasets. During RADEX, the ER-2/CPL sampled above freezing low-level ( $<3 \text{ km}$ ) stratocumulus clouds over the Pacific Ocean off the coast of California and off the coast of Washington. RAP initialization data were used to estimate CTTs, and clear air sampled by the CPL was masked using NASA’s cloud–aerosol detection algorithm noted above (section 3a). A training dataset was developed to separate cloud water and cloud ice based on lidar and thermodynamic measurements using the combined datasets for all columns from the IMPACTS and RADEX research flights using the methodology described below:

To isolate elements composed entirely of cloud liquid water ( $L$ ), all columns where cloud top was detected and CTTs were  $>0^\circ\text{C}$  were isolated. CTTs  $> 0^\circ\text{C}$  were composed only of liquid. The  $\delta$  versus  $\beta$  were recorded from each of the first 10 consecutive elements below the aircraft not masked as clear air. The data from these 10 elements from each of the columns satisfying the above criteria together made up the liquid portion of the training dataset. These data typically had low  $\delta$  and high  $\beta$  (Fig. 8a). The bin widths for Figs. 8a–c were 0.005  $\delta$  and  $\beta$  of  $0.05 \text{ m}^{-1} \text{ sr}^{-1}$ .

To isolate elements composed entirely of cloud ice ( $I$ ), periods during the IMPACTS and RADEX field campaign were isolated where model estimated CTTs were  $<-40^\circ\text{C}$ , the homogeneous freezing temperature of ice. The first 10 consecutive elements below the aircraft were assumed to represent cloud ice and their corresponding  $\delta$  and  $\beta$  were recorded. These elements made up the ice portion of the training dataset in Fig. 8b. These data typically had higher  $\delta$  and lower  $\beta$  than the liquid training dataset (Fig. 8a).

### c. Probability and phase classification

The training dataset was then gridded into coarser bins in order to include more training dataset samples in a given bin

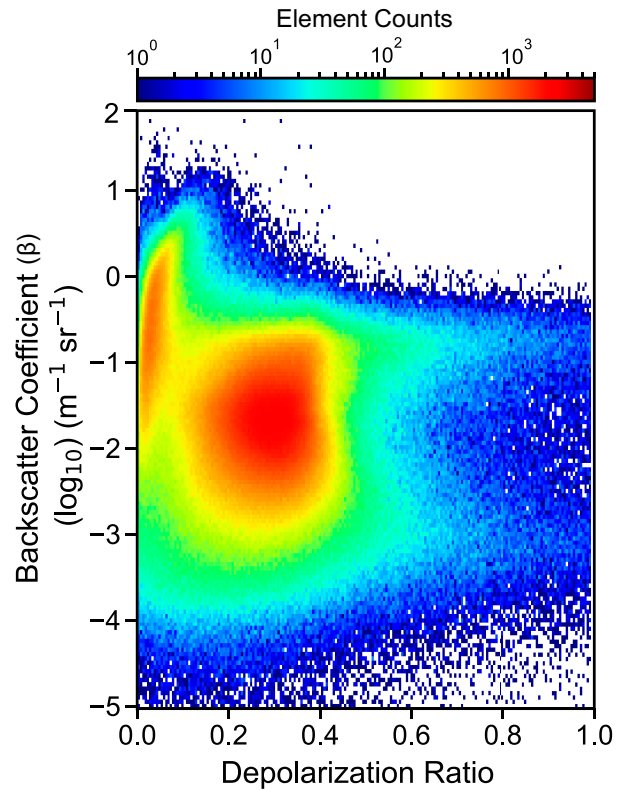


FIG. 7. Two-dimensional histogram showing 1064 nm depolarization ratio ( $\delta$ ) vs 1064 nm backscatter coefficient ( $\beta$ ) of all elements from the 2020, 2022, and 2023 IMPACTS deployments. The bin width was 0.005 for  $\delta$  and  $0.05 \text{ m}^{-1} \text{ sr}^{-1}$  for  $\beta$ .

with column ( $i$ ) increments of 0.025  $\delta$  and row ( $j$ ) dimensions of  $0.25 \text{ m}^{-1} \text{ sr}^{-1} \beta$  (Figs. 8d–f), with each bin containing  $L_{(i,j)}$  (number of liquid elements in a given gridded bin) and  $I_{(i,j)}$  (number of ice elements in a given gridded bin). Bins with  $L_{(i,j)} + I_{(i,j)} < 30$  were excluded. The fraction of liquid elements [ $m_{L(i,j)}$ ] and ice elements [ $m_{I(i,j)}$ ] were then calculated in the remaining bins as

$$m_{L(i,j)} = \frac{L_{(i,j)}}{\sum_i \sum_j L_{(i,j)}}, \quad m_{I(i,j)} = \frac{I_{(i,j)}}{\sum_i \sum_j I_{(i,j)}}.$$

Then, if  $(m_{L(i,j)})/(m_{L(i,j)} + m_{I(i,j)}) > 0.95$ , lidar elements within that bin were assumed to be dominated by liquid. Similarly, if  $(m_{I(i,j)})/(m_{L(i,j)} + m_{I(i,j)}) > 0.95$ , lidar elements were assumed to be dominated by ice. The term “dominated by” is used here to recognize that the classification of an element as liquid does not imply that there was no ice in the cloud element, or liquid in a cloud element classified as ice. The classification represents the dominant phase in that element based on the lidar measurements at 1064 nm. Bins falling outside the training dataset with temperatures  $> -40^\circ\text{C}$ , and bins where the 0.95 threshold was not met were classified as *uncertain*. If an element fell outside of the training datasets but had a temperature  $< -40^\circ\text{C}$ , it was classified as ice. Figure 9 shows

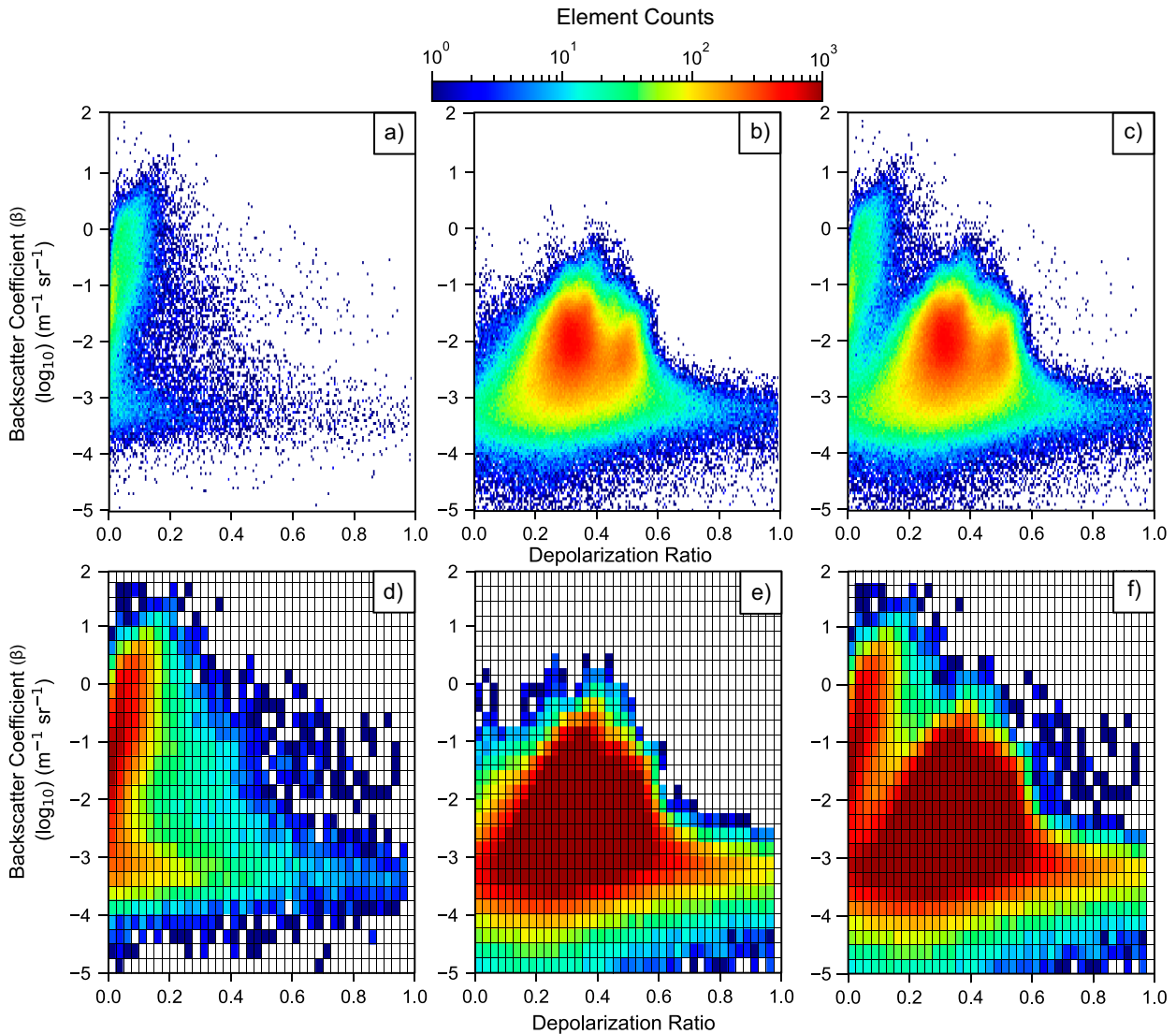


FIG. 8. Two-dimensional histograms of the training dataset: (a) cloud liquid, (b) cloud ice, and (c) cloud liquid and cloud ice. The bin width for (a)–(c) was  $0.005 \delta$  and  $\beta$  of  $0.05 \text{ m}^{-1} \text{ sr}^{-1}$ . (d)–(f) The training dataset was gridded such that each bin has a  $\delta$  of  $0.025$  and  $\beta$  of  $0.25 \text{ m}^{-1} \text{ sr}^{-1}$ . Bins containing less than 30 elements were not used in the training dataset.

phase probability in each  $(i, j)$  bin for liquid, ice, and both training datasets combined. Figure 10 shows the final phase classification when the 0.95 threshold was used. Figure 4f shows an example from 7 February 2020 of the resulting phase identification after classification for all elements.

#### d. Yorks et al. (2011b) and Zaremba et al. (2023) algorithm comparison

This subsection presents a comparison of the NASA default phase algorithm presented in Yorks et al. (2011b) (Y\_2011) and the phase algorithm presented in this manuscript (Z\_2023). Table 2 and Fig. 11 summarize the comparison; 70.9% (156 829) of the cloud-top elements were classified the same by both algorithms. Here we focus on the 29.1% (64 329) of bins that

were not classified as the same phase by both algorithms, primarily liquid phase clouds detected by the Z\_2023 algorithm, but ice phase by Y\_2011. The algorithms primarily disagreed because of the temperature dependence of Y\_2011, resulting in a distinct pattern: agreement in algorithm classification was primarily noted at temperatures below  $-35^\circ\text{C}$  (ice classification), while disagreement was more prevalent in the temperature range of  $-20^\circ$  to  $-35^\circ\text{C}$  (liquid classification).

Cloud-top elements where ice was classified using Y\_2011 but classified as liquid using Z\_2023 were found to have depolarization ratios  $> 0.1$  and backscatterers that ranged from  $10^{-4}$  to  $10^{-1} \text{ m}^{-1} \text{ sr}^{-1}$  (Fig. 11a) outside of the Z\_2023 liquid training dataset. Cloud-top elements where liquid was classified using Z\_2023 but were classified as ice by Y\_2011 were found to have depolarization ratios  $< 0.1$  and backscatter

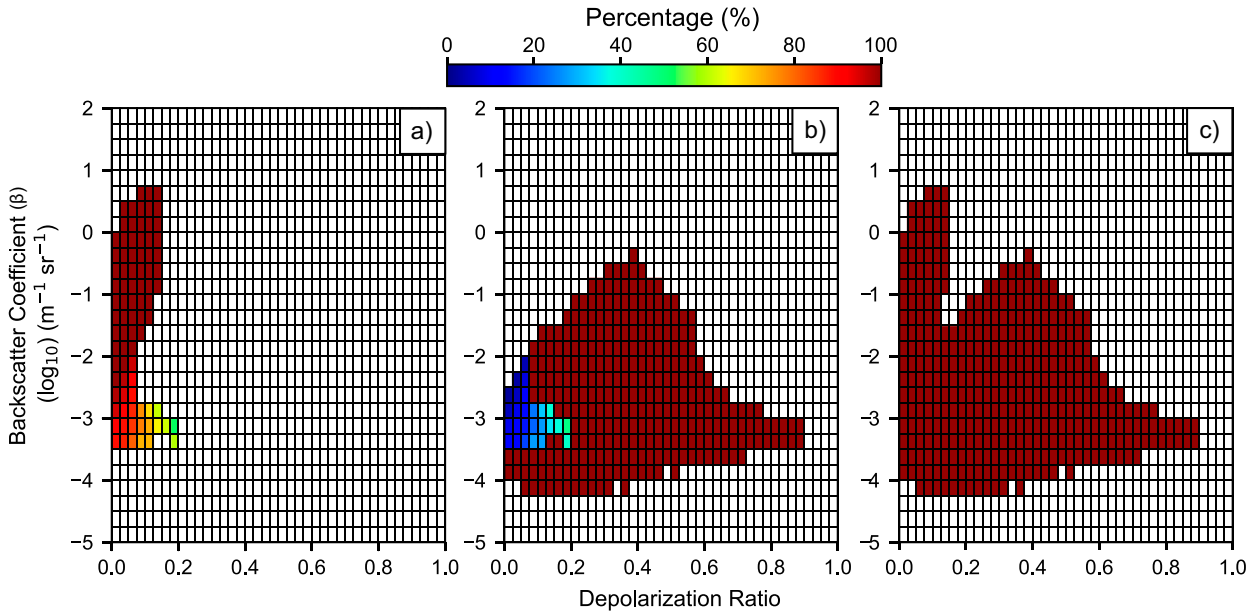


FIG. 9. Probability calculated using methodology discussed in section 4c for (a) liquid, (b) ice, and (c) both liquid and ice.

coefficients ranging between  $10^{-3}$  and  $10^{-1} \text{ m}^{-1} \text{ sr}^{-1}$  (Fig. 11b) falling within the Z\_2023 liquid training dataset. The Y\_2011 algorithm underestimated cloud-top elements classified as liquid by 50% because of its hard cutoff for CTTs  $< -20^\circ\text{C}$ . Elements classified by Z\_2023 as uncertain but as liquid by Y\_2011 typically fell just outside the boundary of the liquid training dataset

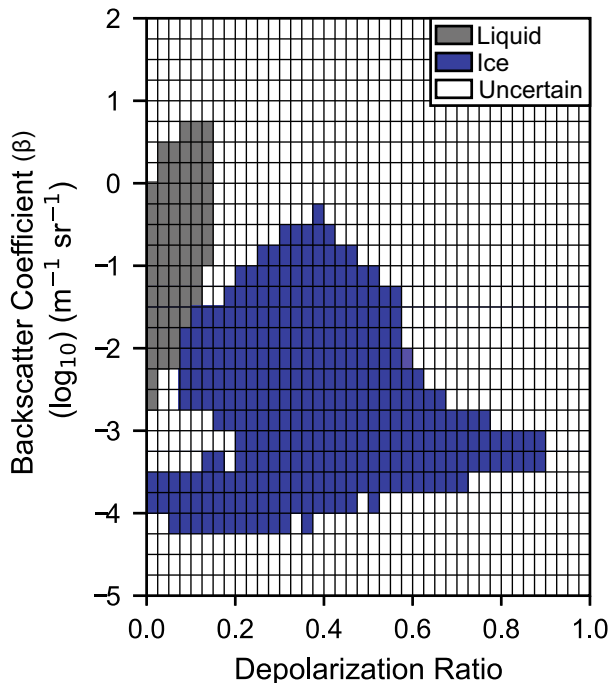


FIG. 10. Final phase classification based on a probability threshold  $> 0.95$  for cloud liquid and cloud ice. Points falling outside of the training datasets with temperatures  $< -40^\circ\text{C}$  were classified as ice.

(having backscatter values  $> 10^\circ$  or  $< 10^{-3} \text{ m}^{-1} \text{ sr}^{-1}$  and depolarization ratios  $< 0.1$ ) and elements classified as ice by Y\_2011 typically fell just outside the ice training dataset (having backscatter  $< 10^{-2} \text{ m}^{-1} \text{ sr}^{-1}$  and depolarization ratios  $> 0.1$ ) (Figs. 11c,d). The comparison between the Y\_2011 and Z\_2023 phase algorithms highlight significant discrepancies in the classification of cloud-top elements, with Y\_2011 often classifying elements differently due to its specific temperature thresholds and depolarization ratio cutoffs, leading to underestimation of liquid elements in extratropical cyclone cloud tops compared to the current algorithm. The discrepancies presented here can help improve the CPL algorithms and inform the algorithm development efforts for future space-based lidar instruments that will fly as part of the NASA Earth System Observatory (ESO) Atmosphere Observing System (AOS) mission.

## 5. Cloud-top phase characteristics

### a. Cloud-top identification and overview statistics

To isolate the cloud-top region in profiles where cloud was present below the aircraft, the first unmasked bin below the aircraft and the four bins directly beneath it (representing the

TABLE 2. Cloud-top comparison between the Yorks et al. (2011b) algorithm and the Zaremba et al. (2023) algorithm presented in this manuscript. The number of elements is in parenthesis.

Zaremba et al. (2023)	Yorks et al. (2011b)		
	Ice	Liquid	Unknown
Ice (137 813)	98.5% (135 804)	1.3% (1790)	0.2% (219)
Liquid (42 453)	50.7% (21 539)	49.2% (20 878)	0.1% (36)
Unknown (40 931)	85.5% (34 997)	14.0% (5748)	0.5% (186)

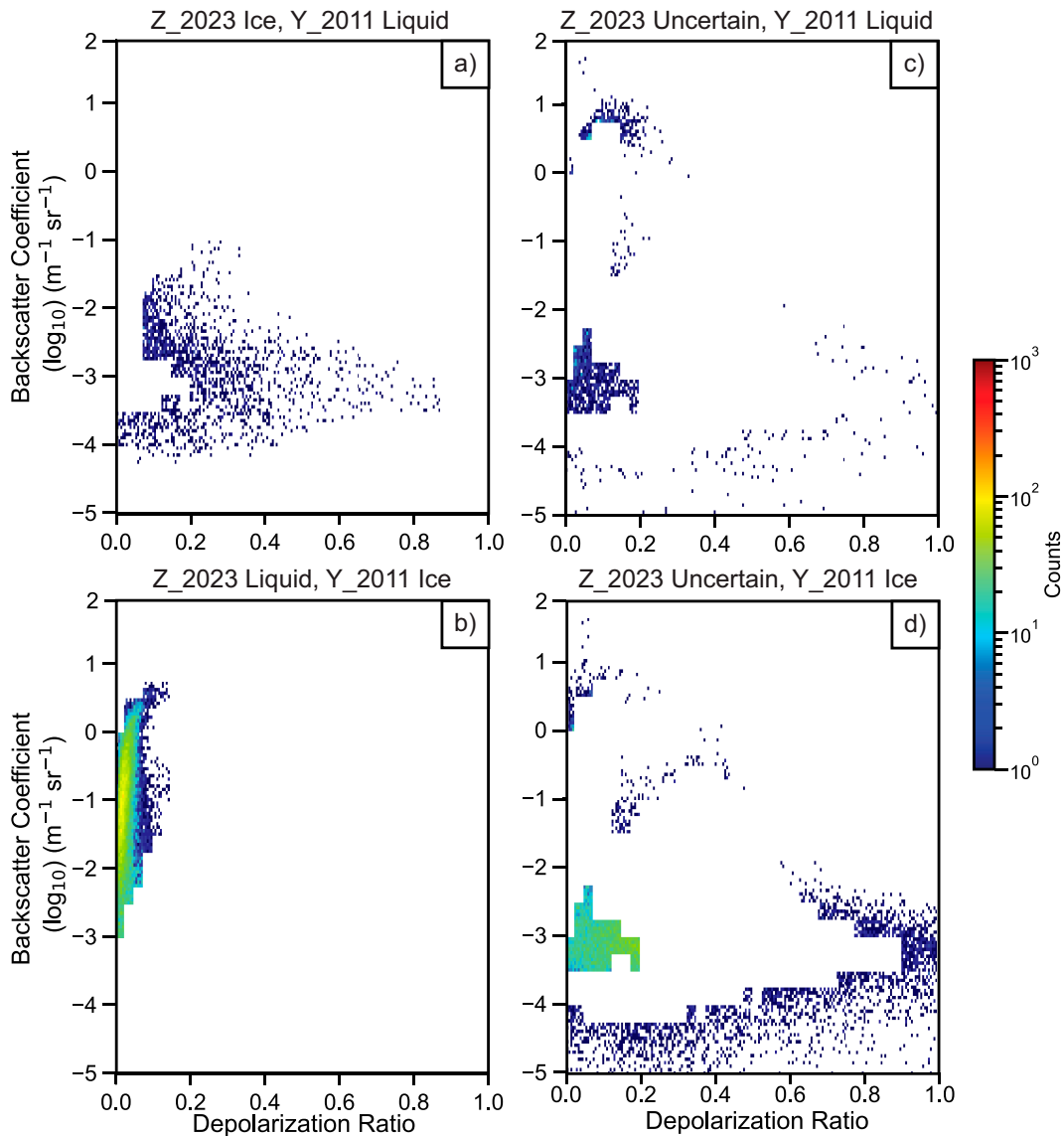


FIG. 11. Comparison of the [Yorks et al. \(2011b\)](#) and the [Zaremba et al. \(2023, this manuscript\)](#) CPL cloud phase algorithms. (a)–(d) Two-dimensional histograms of (a) Z\_2023 ice, Y\_2011 liquid, (b) Z\_2023 liquid, Y\_2011 ice, (c) Z\_2023 uncertain, Y\_2011 liquid, and (d) Z\_2023 uncertain, Y\_2011 ice. Two comparisons, Z\_2023 ice, Y\_2011 uncertain and Z\_2023 liquid, Y\_2011 uncertain had very limited data and are not shown. Bin widths were 0.005  $\delta$  and  $\beta$  of 0.05 m<sup>-1</sup> sr<sup>-1</sup>.

top 150 m of cloud) were considered cloud top. The temperature, estimated from RAP analysis data, and phase of each cloud-top element was recorded. [Figures 4f–h](#) show an example of the final CTP identification from 7 February 2020.

During IMPACTS, 44415 profiles were sampled, 95.1% of which had cloud tops detectable beneath the aircraft associated with extratropical cyclone cloud cover. [Table 3](#) contains information about the number of profiles sampled on each

TABLE 3. Phase of elements beneath cloud top corresponding to [Fig. 12a](#).

Cloud phase	Cloud-top element					All
	1 (0–30 m)	2 (30–60 m)	3 (60–90 m)	4 (90–120 m)	5 (120–150 m)	
Liquid	11.6%	20.1%	21.5%	21.5%	21.2%	19.2%
Ice	50.2%	61.2%	65.1%	66.9%	67.8%	62.3%
Uncertain	38.2%	18.7%	13.3%	11.4%	10.9%	18.5%

research flight where cloud top was sampled beneath the aircraft; 97.2% of cloud-containing columns had cloud top with five consecutive elements (Fig. 12). In some cases, detected clouds were less than 150 m in depth (based on lidar-derived measurements), due to complete attenuation of the lidar signal after cloud-top penetration. Of the cloud-containing columns, 2.8% had lidar detected cloud-top depths less than 150 m. Only 1–4 consecutive bins were present beneath the initial cloud-top bin in these cases (Fig. 12a). The phase of bins as a function of depth within the cloud-top region is presented in Fig. 12b and summarized in Table 3. All columns where cloud was detected were included in the statistical analysis which follows. After cloud-top identification, 81.5% of all cloud-top bins sampled were found to be classified as either dominated by liquid or dominated by ice with the majority of cloud-top bins being classified as ice (62.3%) at depths up to 150 m beneath cloud top. Of all the cloud-top bins sampled, 18.5% were classified as uncertain. These bins were unidentifiable based on the training dataset and probability threshold noted in the previous section. The first vertical bin classified as cloud top was more likely to be classified as uncertain (38.2%, Table 3). These elements typically had lower backscatter than the ice and liquid training datasets and were likely inhomogeneous pixels (cloud + aerosol) along cloud-top boundaries sampled.

### b. CTP in different CTT ranges

During the IMPACTS field campaign, supercooled cloud tops were observed at CTTs ranging from  $-3^{\circ}$  to  $-37^{\circ}\text{C}$ . For example, on 19 January 2022, supercooled cloud tops were observed associated with cloud-top generating cells that had temperatures between  $-30^{\circ}$  and  $-35^{\circ}\text{C}$  (Fig. 13a). Generating cell occurrence was inferred qualitatively by the presence of conditional instability near cloud top,  $1\text{--}2\text{ m s}^{-1}$  upward and downward vertical motions in the radial velocity data, and regions of locally high reflectivity from which a trail of hydrometeors originates extending from cloud top (Figs. 13a,b). This occurred during the passage of an Alberta clipper system across northern New York and southern Canada. Cloud tops identified by the CPL between 1608 and 1612 UTC exhibited high  $\beta$  values ( $> -10^{-3}\text{ m}^{-1}\text{ sr}^{-1}$ ) and low  $\delta$  values ( $< 0.1$ ) indicative of liquid present at cloud top (Figs. 13c–e). Weak vertical motions from the CRS ( $1\text{--}2\text{ m s}^{-1}$ ) were also observed near the cloud top in a potentially unstable layer (where  $\theta_e$  was decreasing with height), resulting in ice formation and precipitation from the generating cells with supercooled liquid cloud tops, evidenced by fall streaks extending from cloud top (Fig. 13a). Between 1602 and 1607 UTC vertical motions were weaker ( $\sim 0\text{ m s}^{-1}$ ) near the cloud top; the cloud top was glaciated and predominantly composed of ice. This was a notable instance of SLW forming at lower CTTs ( $< -30^{\circ}\text{C}$ ) during IMPACTS.

On 27 February 2020, a low pressure system moved into the eastern Great Lakes region, while a secondary cyclone developed over New England, resulting in a Miller type-B storm. The storm was accompanied by cloud-top generating cells that formed in a potentially unstable layer where  $\theta_e$  was decreasing with height and the cloud-top region exhibited vertical

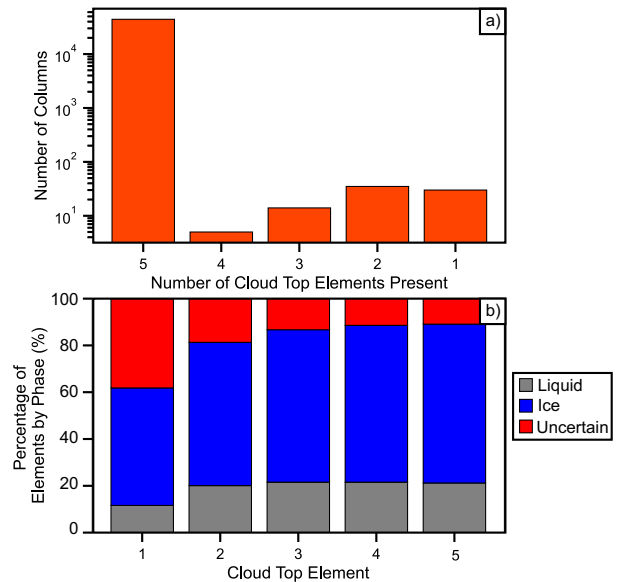


FIG. 12. (a) Number of elements present in the cloud-top layer. Five elements present indicates a cloud-top depth of 150 m. Clouds with less than five elements represent thin or attenuating cloud tops with depths less than 150 m. (b) Normalized percentage of phase detected in each of the five-volume elements making up the cloud top with 1 at the top and 5 at the base of the cloud-top layer (see Table 3).

motions of  $1\text{--}2\text{ m s}^{-1}$  (Figs. 14a,b). Cloud tops varied along the flight leg between 3 and 6 km, with cloud-top generating cells having temperatures between  $-21^{\circ}$  and  $-30^{\circ}\text{C}$ . Clouds farther west (1259–1300) experienced little to no vertical motions at the cloud top and were glaciated with  $\beta$  values of  $10^{-2}$  to  $10^{-3}\text{ m}^{-1}\text{ sr}^{-1}$  and higher  $\delta$  values ( $> 0.1$ ) (Figs. 14c–f).

On 25 February 2020, a shallow and weakly forced storm was observed over Illinois. This system, initially a Great Plains cyclone, later transitioned into the Miller type-B cyclone in Fig. 14. The cloud on 25 February was typically less than 5 km deep and featured cloud-top generating cells and elevated convective cells with updraft and downdraft magnitudes of approximately  $\pm 3\text{ m s}^{-1}$  at the cloud top (Figs. 15a,b). The CTTs in this case ranged from  $-3^{\circ}$  to  $-20^{\circ}\text{C}$ . The dominance of liquid cloud tops in this case was likely due to stronger vertical motions and warmer CTTs with cloud tops exhibiting high  $\beta$  values ( $> -10^{-3}\text{ m}^{-1}\text{ sr}^{-1}$ ) and low  $\delta$  values ( $< 0.1$ ) (Figs. 15c–f).

These three case studies illustrate that the presence of liquid at cloud top depends both on CTT and the presence of vertical motions near cloud top.

### c. Cloud-top phase characterization summary

During IMPACTS the ER-2 sampled along a given flight track deep stratiform cloud cover that often had cloud-top generating cells if potential instability was present, stratiform tops without generating cells, or elevated convection associated with potential instability above frontal surfaces (e.g., Varcie et al. 2023). Figure 1 shows the typical flight tracks flown during different events and examples of typical cloud

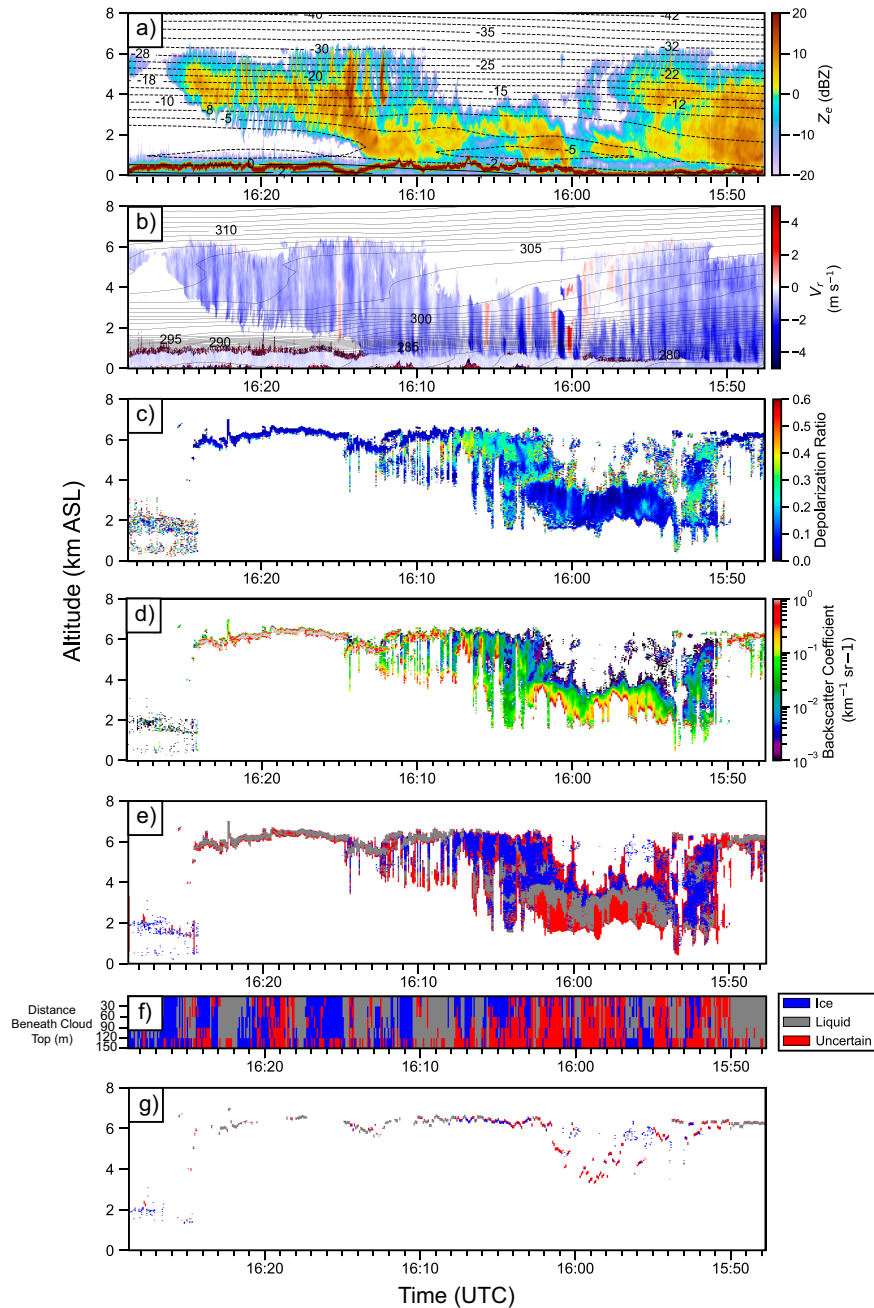


FIG. 13. Flight leg from 1547:40 to 1628:50 UTC 19 Jan 2022. This storm system was an Alberta clipper. (a) Two Hz CRS  $Z_e$  overlaid with temperature data (in  $^{\circ}\text{C}$ ) from RAP analysis data valid at 1600 UTC, (b) 2 Hz CRS  $V_r$  overlaid with RAP analysis equivalent potential temperature (in K), (c) CPL  $\delta$ , (d) CPL  $\beta$ , (e) CPL phase classification (blue is ice, gray is liquid, and red is uncertain), and (f) CTP classification (top 150 m, first five bins). Each bin represents 30 m. This corresponds to the first five elements identified as cloud top in (g). (g) CTP (top 150 m).

expand from *GOES-16* over the northeast United States. In this section, CTP was quantified as a function of CTT for all extratropical cyclones sampled by the ER-2 during IMPACTS research flight legs (the ferry legs to and from the storm are excluded).

Figure 16 illustrates the relationship between CTT and CTP for all research flights. Final CTP classification was determined by finding the most frequently occurring phase among the first five cloud-top elements. The analysis of the IMPACTS dataset reveals that 99.4% of the sampled cloud

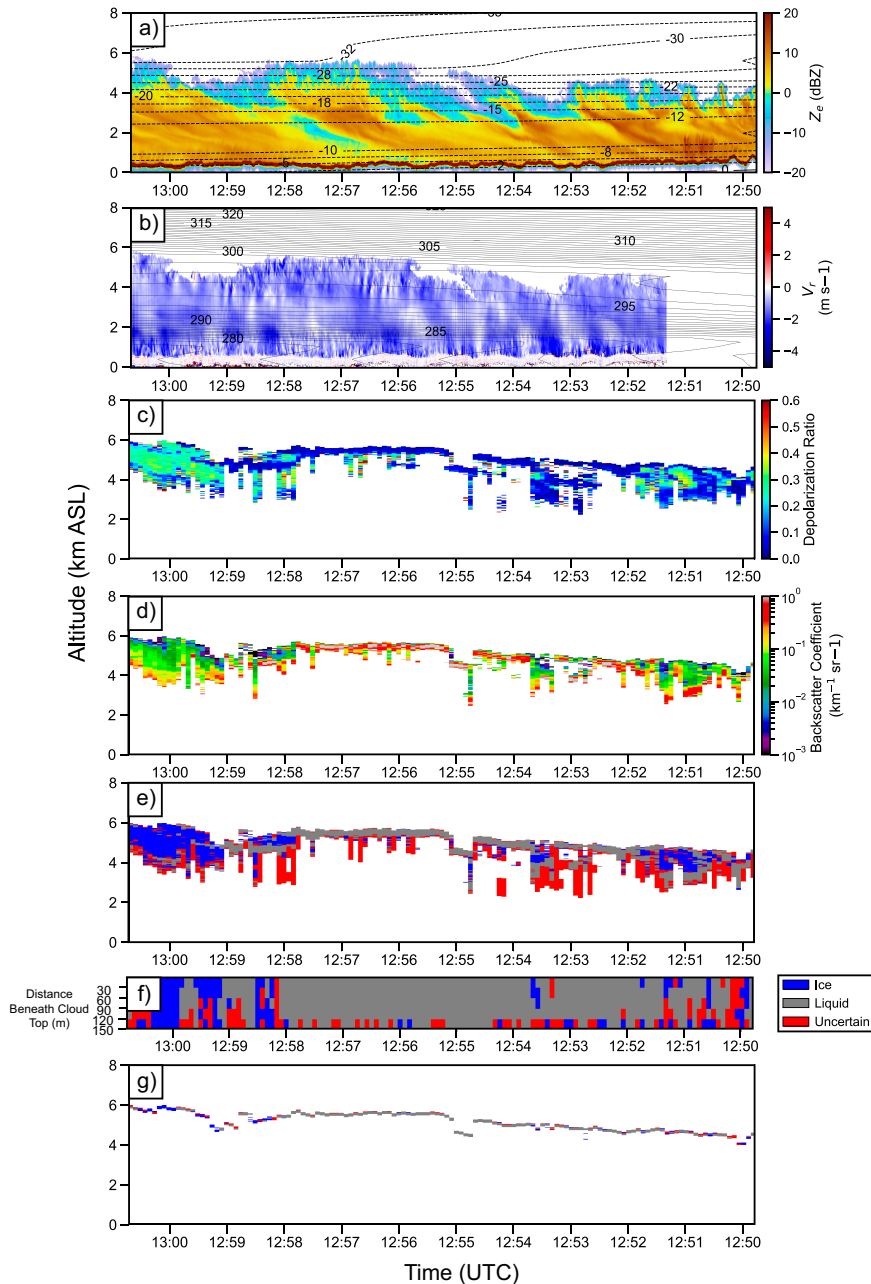


FIG. 14. As in Fig. 13, but for a flight leg between 1249:49 and 1300:50 UTC 27 Feb 2020. This storm system was a Miller type-B cyclone.

profiles had CTTs  $< 0^{\circ}\text{C}$ . Of these, 59.4% of clouds had CTTs  $< -40^{\circ}\text{C}$ , beneath the homogenous freezing temperature of ice. 39.6% of clouds sampled had CTTs  $> -40^{\circ}\text{C}$ . Within this subset, 21.5% were dominated by liquid cloud tops, and 71.6% were dominated by ice cloud tops (Table 4). Notably, Fig. 16 displays the presence of liquid cloud-top elements even at CTTs as low as  $-37^{\circ}\text{C}$ . No SLW was found at CTTs  $< -37^{\circ}\text{C}$ . Approximately 3.5% of the sampled cloud top with CTTs ranging from  $-35^{\circ}$  to  $-40^{\circ}\text{C}$  were dominated by SLW at cloud top. As CTT increased, the frequency of

liquid cloud tops also increased. Specifically, between  $-30^{\circ}$  and  $-35^{\circ}\text{C}$ , 39.6% of cloud tops were identified as liquid, with percentages of 55.7% between  $-25^{\circ}$  and  $-30^{\circ}\text{C}$ , 62.3% between  $-20^{\circ}$  and  $-25^{\circ}\text{C}$ , and 72.5% between  $-15^{\circ}$  and  $-20^{\circ}\text{C}$ . The highest frequency of liquid cloud tops, at 85.1%, occurred between  $-10^{\circ}$  and  $-15^{\circ}\text{C}$ . Interestingly, the percentage of ice-dominated cloud tops increased at temperatures  $> -10^{\circ}\text{C}$ . These temperatures correspond to regions where secondary ice production mechanisms are common (Field et al. 2017). This analysis demonstrates that a significant portion of cloud tops

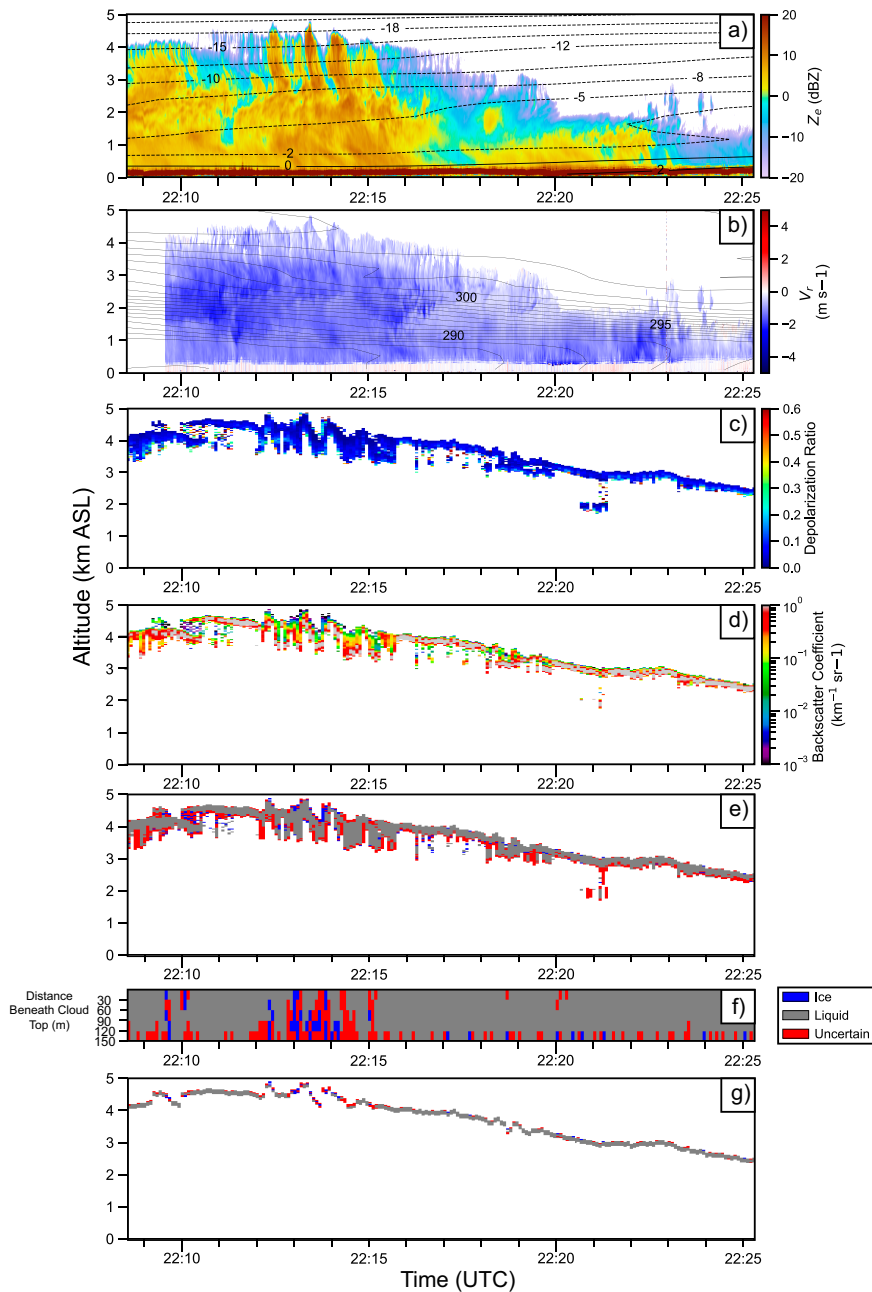


FIG. 15. As in Fig. 13, but for a flight leg between 2208:34 and 2225:20 UTC 25 Feb 2020. This storm system was a Great Plains cyclone.

observed over the northeast and midwest United States in cyclones during IMPACTS exhibited SLW at CTTs > -30°C, with a higher occurrence at temperatures > -20°C.

### 6. Discussion

IMPACTS provided critical insights into the CTP of extratropical cyclones over the northeast and midwest United States, revealing that a significant fraction of cloud tops exhibit SLW at CTTs > -30°C. These findings align with

previous research, such as Plummer et al. (2014), who documented the presence of SLW within cloud-top generating cells during a limited number of in situ cloud-top samples. Our extensive remote sensing dataset supports these earlier observations, indicating that the presence of SLW is not only common but also persists down to temperatures as low as -35° to -37°C, depending on the accuracy of the RAP temperature fields.

Ice formation often occurs in the cloud-top region of stratiform clouds where 1–2 m s<sup>-1</sup> updrafts produce supercooled

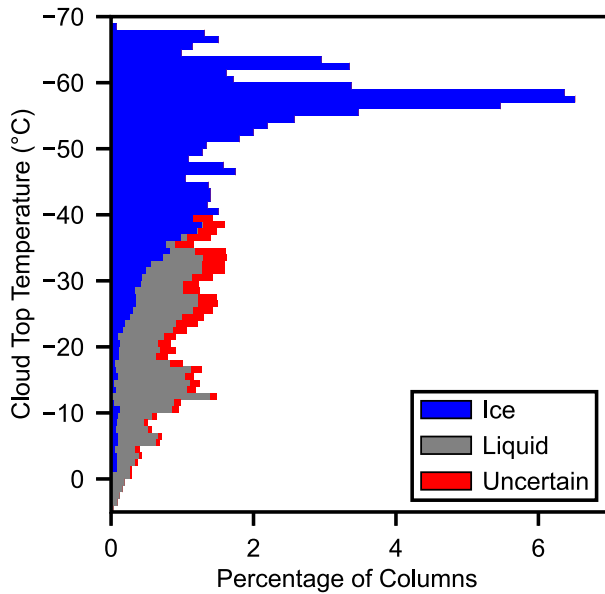


FIG. 16. Cloud-top phase as a function of CTT for all columns sampled during IMPACTS (see Table 4).

water droplets and are associated with cloud-top generating cells (e.g., Rosenow et al. 2014; Plummer et al. 2014, 2015). These droplets permit efficient ice nucleation pathways such as contact nucleation and immersion freezing nucleation (e.g., Young 1974) within what is typically the coldest region of the cloud. This study's observations of SLW at cloud top confirm that the updraft intensity within generating cells is sufficient to maintain SLW as predicted Rauber and Tokay (1991), even at temperatures nearing that required of homogeneous freezing.

The implications of our findings extend to climate modeling. In extratropical cyclones, the cloud phase is a key factor in determining cloud radiative forcing, particularly at cloud top. In this analysis, liquid was observed at cloud top more than 50% of the time at temperatures  $> -30^{\circ}\text{C}$ . The critical temperature threshold at which ice and liquid are equally probable varies considerably in climate models depending on the parameterizations used. For example, the parameterization introduced by Del Genio et al. (1996, their Fig. 2) shows

that the 50% critical temperature threshold was  $-17^{\circ}\text{C}$  in clouds over land. Naud et al. (2006) found that the critical temperature was variable relative to composited cyclone centers. Critical temperature thresholds, as discussed by Del Genio et al. (1996) and Naud et al. (2006), provide a benchmark for model intercomparisons. We note that the Del Genio et al. (1996) parameterization applies to mixed-phase clouds throughout the cloud depth. Our results only apply to the cloud top, which is a unique environment because ice particles begin their growth there and are small, and updrafts within generating cells are unusually strong compared to the body of the stratiform cloud below (Rauber and Tokay 1991; Rosenow et al. 2014; Keeler et al. 2017). Nevertheless, because of the importance of cloud top in both cloud radiative forcing and ice nucleation, it is important that both climate and forecasting models accurately depict cloud-top phase. Our observations underscore the importance of accurately representing CTP correctly in climate models, given CTP's impact on the broader climate system.

## 7. Conclusions

This study used airborne remote sensing observations to determine and statistically represent cloud-top phase (CTP) of extratropical cyclones over the northeast and midwest United States. The main question addressed by this study was what percentage of cloud tops sampled during the Investigation of Microphysics and Precipitation for Atlantic Coast-Threatening Snowstorms (IMPACTS) had supercooled liquid water (SLW) present at cloud top as a function of cloud-top temperature (CTT). A training dataset was developed for cloud liquid and cloud ice to create probabilistic classifications based on Cloud Physics Lidar data. These classifications were used to differentiate between liquid and ice cloud tops and characterize CTP. Case studies were presented illustrating examples of SLW at cloud top at different ranges of CTTs ( $-3^{\circ} < \text{CTT} < -35^{\circ}\text{C}$ ).

The analysis of the IMPACTS dataset reveals that 99.4% of the sampled cloud columns had CTTs  $< 0^{\circ}\text{C}$ . Of these, 59.4% of clouds had CTTs  $< -40^{\circ}\text{C}$ , beneath the homogeneous freezing temperature of ice; 39.6% of clouds sampled had CTTs  $> -40^{\circ}\text{C}$ . Within this subset, 21.5% were dominated by liquid cloud tops, and 71.6% were dominated by ice

TABLE 4. CTP as a function of CTT.

Cloud-top temperature	Liquid	Ice	Unknown	Number of cloud-top bins	Number of cloud-top profiles	Percentage of cloud-top profiles
$< -40^{\circ}\text{C}$	0%	100%	0%	132 883	26 237	59.1%
$-40^{\circ}$ to $-35^{\circ}\text{C}$	3.5%	76.3%	20.1%	14 588	2919	6.5%
$-35^{\circ}$ to $-30^{\circ}\text{C}$	39.6%	38.8%	21.5%	16 203	3244	7.3%
$-30^{\circ}$ to $-25^{\circ}\text{C}$	55.7%	25.9%	18.3%	14 161	2833	6.3%
$-25^{\circ}$ to $-20^{\circ}\text{C}$	62.3%	16.7%	20.9%	10 981	2197	4.9%
$-20^{\circ}$ to $-15^{\circ}\text{C}$	75.2%	8.7%	16%	10 564	2122	4.7%
$-15^{\circ}$ to $-10^{\circ}\text{C}$	85.1%	5.5%	9.3%	12 006	2417	5.4%
$-10^{\circ}$ to $-5^{\circ}\text{C}$	77.0%	14.7%	8.2%	6419	1287	2.9%
$-5^{\circ}$ to $0^{\circ}\text{C}$	64.3%	25.6%	9.8%	3679	745	1.7%
$> 0^{\circ}\text{C}$	100%	0%	0%	1410	287	0.6%

cloud tops. Liquid cloud-top elements were observed at CTTs as low as  $-37^{\circ}\text{C}$ . Approximately 3.5% of the sampled cloud tops with CTTs ranging from  $-35^{\circ}$  to  $-40^{\circ}\text{C}$  were dominated by SLW. As CTTs increased, the frequency of liquid cloud tops also increased. Specifically, between  $-30^{\circ}$  and  $-35^{\circ}\text{C}$ , 39.6% of cloud tops were identified as liquid, with percentages of 55.7% between  $-25^{\circ}$  and  $-30^{\circ}\text{C}$ , 62.3% between  $-20^{\circ}$  and  $-25^{\circ}\text{C}$ , and 72.5% between  $-15^{\circ}$  and  $-20^{\circ}\text{C}$ . The highest frequency of liquid cloud tops, at 85.1%, occurred between  $-10^{\circ}$  and  $-15^{\circ}\text{C}$ .

IMPACTS provided new insight into extratropical cyclone CTP through the use of airborne cloud radar, lidar, and thermodynamic observations. More theoretical, observational, and modeling studies are required to understand the distribution and processes that maintain and sustain SLW at cloud top within extratropical cyclones. Future work should aim to look at better understanding the dynamics of cloud-top generating cells and how ice is produced within them. During IMPACTS, there were very few instances where the P-3 flew through cloud top to collect microphysical information about this region of cloud. In future field campaigns, there should be concerted efforts to sample extratropical cyclone cloud tops to investigate the spatial distribution of liquid and glaciated cloud tops, cloud-top generating cells, and elevated convective cells within winter storms.

*Acknowledgments.* Field campaigns of this size depend on the dedication and support of many individuals and institutions. We thank everyone involved in the planning, execution, and support of the IMPACTS field campaign. We also thank the NASA Earth Science Division (ESD) and Earth Venture Suborbital Program under the NASA Airborne Science Program for their support of this program. We especially thank the crews from the NASA P-3 Orion and the NASA Earth Resources 2 aircrafts. This work was funded by the NASA Earth Venture Suborbital-3 (EVS-3) program under Grants 80NSSC19K0355 (UIUC), 80NSSC19K0338 (UW), and 80NSSC19K0399 (OU). We also thank Dr. Ali Tokay and two anonymous reviewer's for comments and suggestions that helped substantially improve the quality of the paper.

*Data availability statement.* All IMPACTS quick-look images and mission scientist reports from the 2020, 2022, and 2023 deployment are highlighted in the IMPACTS field catalog at [https://www.eol.ucar.edu/field\\_projects/impacts](https://www.eol.ucar.edu/field_projects/impacts) and the data can be obtained from the Global Hydrology Resource Center Distributed Active Archive Center at [https://ghrc.nsstc.nasa.gov/uso/ds\\_details/collections/impactsC.html](https://ghrc.nsstc.nasa.gov/uso/ds_details/collections/impactsC.html) and McMurdie et al. (2019).

## REFERENCES

- Ansmann, A., H. Baars, M. Tesche, D. Müller, D. Althausen, R. Engelmann, T. Pauliquevis, and P. Artaxo, 2009: Dust and smoke transport from Africa to South America: Lidar profiling over Cape Verde and the Amazon rainforest. *Geophys. Res. Lett.*, **36**, L11802, <https://doi.org/10.1029/2009GL037923>.
- Benjamin, S. G., and Coauthors, 2016: A North American hourly assimilation and model forecast cycle: The Rapid Refresh. *Mon. Wea. Rev.*, **144**, 1669–1694, <https://doi.org/10.1175/MWR-D-15-0242.1>.
- Carbone, R. E., and A. R. Bohne, 1975: Cellular snow generation—A Doppler radar study. *J. Atmos. Sci.*, **32**, 1384–1394, [https://doi.org/10.1175/1520-0469\(1975\)032<1384:CSGDRS>2.0.CO;2](https://doi.org/10.1175/1520-0469(1975)032<1384:CSGDRS>2.0.CO;2).
- de Boer, G., H. Morrison, M. D. Shupe, and R. Hildner, 2011: Evidence of liquid dependent ice nucleation in high-latitude stratiform clouds from surface remote sensors. *Geophys. Res. Lett.*, **38**, L01803, <https://doi.org/10.1029/2010GL046016>.
- Del Genio, A. D., M.-S. Yao, W. Kovari, and K. K.-W. Lo, 1996: A prognostic cloud water parameterization for global climate models. *J. Climate*, **9**, 270–304, [https://doi.org/10.1175/1520-0442\(1996\)009<0270:APCWPF>2.0.CO;2](https://doi.org/10.1175/1520-0442(1996)009<0270:APCWPF>2.0.CO;2).
- Douglas, R. H., K. L. S. Gunn, and J. S. Marshall, 1957: Pattern in the vertical of snow generation. *J. Meteor.*, **14**, 95–114, [https://doi.org/10.1175/1520-0469\(1957\)014<0095:PITVOS>2.0.CO;2](https://doi.org/10.1175/1520-0469(1957)014<0095:PITVOS>2.0.CO;2).
- Field, P. R., and Coauthors, 2001: Ice nucleation in orographic wave clouds: Measurements made during INTACC. *Quart. J. Roy. Meteor. Soc.*, **127**, 1493–1512, <https://doi.org/10.1002/qj.49712757502>.
- , and Coauthors, 2017: Secondary ice production: Current state of the science and recommendations for the future. *Ice Formation and Evolution in Clouds and Precipitation: Measurement and Modeling Challenges*, Meteor. Monogr., No. 58, Amer. Meteor. Soc., <https://doi.org/10.1175/AMSMONOGRAPHIS-D-16-0014.1>.
- Henneberger, J., and Coauthors, 2023: Seeding of supercooled low stratus clouds with a UAV to study microphysical ice processes: An introduction to the CLOUDLAB project. *Bull. Amer. Meteor. Soc.*, **104**, E1962–E1979, <https://doi.org/10.1175/BAMS-D-22-0178.1>.
- Hersbach, H., and Coauthors, 2020: The ERA5 global reanalysis. *Quart. J. Roy. Meteor. Soc.*, **146**, 1999–2049, <https://doi.org/10.1002/qj.3803>.
- Houze, R. A., Jr., and Coauthors, 2017: The Olympic Mountains Experiment (OLYMPEX). *Bull. Amer. Meteor. Soc.*, **98**, 2167–2188, <https://doi.org/10.1175/BAMS-D-16-0182.1>.
- Hu, Y., 2007: Depolarization ratio–effective lidar ratio relation: Theoretical basis for space lidar cloud phase discrimination. *Geophys. Res. Lett.*, **34**, L11812, <https://doi.org/10.1029/2007GL029584>.
- , and Coauthors, 2009: CALIPSO/CALIOP cloud phase discrimination algorithm. *J. Atmos. Oceanic Technol.*, **26**, 2293–2309, <https://doi.org/10.1175/2009JTECHA1280.1>.
- Kanji, Z. A., L. A. Ladino, H. Wex, Y. Boose, M. Burkert-Kohn, D. J. Cziczo, and M. Krämer, 2017: Overview of ice nucleating particles. *Ice Formation and Evolution in Clouds and Precipitation: Measurement and Modeling Challenges*, Meteor. Monogr., No. 58, Amer. Meteor. Soc., <https://doi.org/10.1175/AMSMONOGRAPHIS-D-16-0006.1>.
- Keeler, J. M., B. F. Jewett, R. M. Rauber, G. M. McFarquhar, R. M. Rasmussen, L. Xue, C. Liu, and G. Thompson, 2016a: Dynamics of cloud-top generating cells in winter cyclones. Part I: Idealized simulations in the context of field observations. *J. Atmos. Sci.*, **73**, 1507–1527, <https://doi.org/10.1175/JAS-D-15-0126.1>.
- , —, —, —, —, —, and —, 2016b: Dynamics of cloud-top generating cells in winter cyclones. Part II: Radiative and instability forcing. *J. Atmos. Sci.*, **73**, 1529–1553, <https://doi.org/10.1175/JAS-D-15-0127.1>.

- , R. M. Rauber, B. F. Jewett, G. M. McFarquhar, R. M. Rasmussen, L. Xue, C. Liu, and G. Thompson, 2017: Dynamics of cloud-top generating cells in winter cyclones. Part III: Shear and convective organization. *J. Atmos. Sci.*, **74**, 2879–2897, <https://doi.org/10.1175/JAS-D-16-0314.1>.
- Kumjian, M. R., S. A. Rutledge, R. M. Rasmussen, P. C. Kennedy, and M. Dixon, 2014: High-resolution polarimetric radar observations of snow-generating cells. *J. Appl. Meteor. Climatol.*, **53**, 1636–1658, <https://doi.org/10.1175/JAMC-D-13-0312.1>.
- Liu, Z., M. McGill, Y. Hu, C. Hostetler, M. Vaughan, and D. Winker, 2004: Validating lidar depolarization calibration using solar radiation scattered by ice clouds. *IEEE Geosci. Remote Sens. Lett.*, **1**, 157–161, <https://doi.org/10.1109/LGRS.2004.829613>.
- , and Coauthors, 2009: The CALIPSO lidar cloud and aerosol discrimination: Version 2 algorithm and initial assessment of performance. *J. Atmos. Oceanic Technol.*, **26**, 1198–1213, <https://doi.org/10.1175/2009JTECHA1229.1>.
- Luke, E. P., P. Kollias, and M. D. Shupe, 2010: Detection of supercooled liquid in mixed-phase clouds using radar Doppler spectra. *J. Geophys. Res.*, **115**, D19201, <https://doi.org/10.1029/2009JD012884>.
- McFarquhar, G. M., and Coauthors, 2011: Indirect and Semi-Direct Aerosol Campaign: The impact of Arctic aerosols on clouds. *Bull. Amer. Meteor. Soc.*, **92**, 183–201, <https://doi.org/10.1175/2010BAMS2935.1>.
- McGill, M., D. Hlavka, W. Hart, V. S. Scott, J. Spinhirne, and B. Schmid, 2002: Cloud Physics Lidar: Instrument description and initial measurement results. *Appl. Opt.*, **41**, 3725–3734, <https://doi.org/10.1364/AO.41.003725>.
- McLinden, M. L. W., A. M. Loftus, L. Li, and G. M. Heymsfield, 2021a: Application of nonuniform beam filling (NUBF) Doppler velocity error correction on airborne radar measurements. *IEEE Geosci. Remote Sens. Lett.*, **19**, 3509905, <https://doi.org/10.1109/LGRS.2021.3120647>.
- , L. Li, G. M. Heymsfield, M. Coon, and A. Emory, 2021b: The NASA GSFC 94-GHz airborne solid-state Cloud Radar System (CRS). *J. Atmos. Oceanic Technol.*, **38**, 1001–1017, <https://doi.org/10.1175/JTECH-D-20-0127.1>.
- McMurdie, L. A., G. Heymsfield, J. E. Yorks, and S. A. Braun, 2019: Investigation of Microphysics and Precipitation for Atlantic Coast-Threatening Snowstorms (IMPACTS) collection. NASA EOSDIS Global Hydrology Resource Center Distributed Active Archive Center, accessed 15 May 2023, <https://doi.org/10.5067/IMPACTS/DATA101>.
- , and Coauthors, 2022: Chasing snowstorms: The Investigation of Microphysics and Precipitation for Atlantic Coast-Threatening Snowstorms (IMPACTS) campaign. *Bull. Amer. Meteor. Soc.*, **103**, E1243–E1269, <https://doi.org/10.1175/BAMS-D-20-0246.1>.
- Miller, J. E., 1946: Cyclogenesis in the Atlantic coastal region of the United States. *J. Meteor.*, **3**, 31–44, [https://doi.org/10.1175/1520-0469\(1946\)003<0031:CITACR>2.0.CO;2](https://doi.org/10.1175/1520-0469(1946)003<0031:CITACR>2.0.CO;2).
- Naud, C. M., and B. H. Kahn, 2015: Thermodynamic phase and ice cloud properties in Northern Hemisphere winter extratropical cyclones observed by Aqua AIRS. *J. Appl. Meteor. Climatol.*, **54**, 2283–2303, <https://doi.org/10.1175/JAMC-D-15-0045.1>.
- , A. D. Del Genio, and M. Bauer, 2006: Observational constraints on the cloud thermodynamic phase in midlatitude storms. *J. Climate*, **19**, 5273–5288, <https://doi.org/10.1175/JCLI3919.1>.
- Noel, V., D. M. Winker, M. McGill, and P. Lawson, 2004: Classification of particle shapes from lidar depolarization ratio in convective ice clouds compared to in situ observations during CRYSTAL-FACE. *J. Geophys. Res.*, **109**, D24213, <https://doi.org/10.1029/2004JD004883>.
- Plummer, D. M., G. M. McFarquhar, R. M. Rauber, B. F. Jewett, and D. C. Leon, 2014: Structure and statistical analysis of the microphysical properties of generating cells in the comma head region of continental winter cyclones. *J. Atmos. Sci.*, **71**, 4181–4203, <https://doi.org/10.1175/JAS-D-14-0100.1>.
- , —, —, —, and —, 2015: Microphysical properties of convectively generated fall streaks within the stratiform comma head region of continental winter cyclones. *J. Atmos. Sci.*, **72**, 2465–2483, <https://doi.org/10.1175/JAS-D-14-0354.1>.
- Rauber, R. M., and A. Tokay, 1991: An explanation for the existence of supercooled water at the top of cold clouds. *J. Atmos. Sci.*, **48**, 1005–1023, [https://doi.org/10.1175/1520-0469\(1991\)048<1005:AEFTEO>2.0.CO;2](https://doi.org/10.1175/1520-0469(1991)048<1005:AEFTEO>2.0.CO;2).
- Rosenow, A. A., D. M. Plummer, R. M. Rauber, G. M. McFarquhar, B. F. Jewett, and D. Leon, 2014: Vertical velocity and physical structure of generating cells and convection in the comma head region of continental winter cyclones. *J. Atmos. Sci.*, **71**, 1538–1558, <https://doi.org/10.1175/JAS-D-13-0249.1>.
- Shupe, M. D., 2007: A ground based multisensory cloud phase classifier. *J. Geophys. Res.*, **34**, L22809, <https://doi.org/10.1029/2007GL031008>.
- Silber, I., J. Verlinde, E. W. Eloranta, and M. Cadetdu, 2018: Antarctic cloud macrophysical, thermodynamic phase, and atmospheric inversion coupling properties at McMurdo station: I. Principal data processing and climatology. *J. Geophys. Res. Atmos.*, **123**, 6099–6121, <https://doi.org/10.1029/2018JD028279>.
- Thorsen, T. J., Q. Fu, R. K. Newsom, D. D. Turner, and J. M. Comstock, 2015: Automated retrieval of cloud and aerosol properties from the ARM Raman lidar. Part I: Feature detection. *J. Atmos. Oceanic Technol.*, **32**, 1977–1998, <https://doi.org/10.1175/JTECH-D-14-00150.1>.
- Tridon, F., and Coauthors, 2019: The microphysics of stratiform precipitation during OLYMPEX: Compatibility between triple-frequency radar and airborne in situ observations. *J. Geophys. Res. Atmos.*, **124**, 8764–8792, <https://doi.org/10.1029/2018JD029858>.
- Varcie, M. M., and Coauthors, 2023: Precipitation growth processes in the comma-head region of the 7 February 2020 northeast snowstorm: Results from IMPACTS. *J. Appl. Meteor. Climatol.*, **80**, 3–29, <https://doi.org/10.1175/JAS-D-22-0118.1>.
- Venema, V., H. Russchenberg, A. Apituley, A. van Lammeren, and L. Ligthart, 2000: Cloud boundary height measurements using lidar and radar. *Phys. Chem. Earth*, **25B**, 129–134, [https://doi.org/10.1016/S1464-1909\(99\)00139-2](https://doi.org/10.1016/S1464-1909(99)00139-2).
- Wang, Y., and Coauthors, 2020: Microphysical properties of generating cells over the Southern Ocean: Results from SOCRATES. *J. Geophys. Res. Atmos.*, **125**, e2019JD032237, <https://doi.org/10.1029/2019JD032237>.
- Westbrook, C. D., and A. J. Heymsfield, 2011: Ice crystals growing from vapor in supercooled clouds between  $-2.5^\circ$  and  $-22^\circ\text{C}$ : Testing current parameterization methods using laboratory data. *J. Atmos. Sci.*, **68**, 2416–2429, <https://doi.org/10.1175/JAS-D-11-017.1>.
- , and A. J. Illingworth, 2011: Evidence that ice forms primarily in supercooled liquid clouds at temperatures  $> -27^\circ\text{C}$ . *Geophys. Res. Lett.*, **38**, L14808, <https://doi.org/10.1029/2011GL048021>.
- Wexler, R., 1955: Radar analysis of precipitation streamers observed 25 February 1954. *J. Meteor.*, **12**, 391–393, [https://doi.org/10.1175/1520-0469\(1955\)012<0391:RAOPSO>2.0.CO;2](https://doi.org/10.1175/1520-0469(1955)012<0391:RAOPSO>2.0.CO;2).

- , and D. Atlas, 1959: Precipitation generating cells. *J. Meteor.*, **16**, 327–332, [https://doi.org/10.1175/1520-0469\(1959\)016<0327:PGC>2.0.CO;2](https://doi.org/10.1175/1520-0469(1959)016<0327:PGC>2.0.CO;2).
- Yorks, J. E., D. L. Hlavka, M. A. Vaughan, M. J. McGill, W. D. Hart, S. Rodier, and R. Kuehn, 2011a: Airborne validation of cirrus cloud properties derived from CALIPSO lidar measurements: Spatial properties. *J. Geophys. Res.*, **116**, D19207, <https://doi.org/10.1029/2011JD015942>.
- , —, W. D. Hart, and M. J. McGill, 2011b: Statistics of cloud optical properties from airborne lidar measurements. *J. Atmos. Oceanic Technol.*, **28**, 869–883, <https://doi.org/10.1175/2011JTECHA1507.1>.
- , P. A. Selmer, A. Kupchock, E. P. Nowotnick, K. E. Christian, D. Rusinek, N. Dacic, and M. J. McGill, 2021: Aerosol and cloud detection using machine learning algorithms and space-based lidar data. *Atmosphere*, **12**, 606, <https://doi.org/10.3390/atmos12050606>.
- Young, K. C., 1974: The role of contact nucleation in ice phase initiation in clouds. *J. Atmos. Sci.*, **31**, 768–776, [https://doi.org/10.1175/1520-0469\(1974\)031<0768:TROCNI>2.0.CO;2](https://doi.org/10.1175/1520-0469(1974)031<0768:TROCNI>2.0.CO;2).
- Zaremba, T. J., R. M. Rauber, G. M. McFarquhar, M. Hayman, J. A. Finlon, and D. M. Stechman, 2020: Phase characterization of cold sector Southern Ocean cloud tops: Results from SOCRATES. *J. Geophys. Res. Atmos.*, **24**, e2020JD033673, <https://doi.org/10.1029/2020JD033673>.
- Zhang, J., and Coauthors, 2016: Multi-Radar Multi-Sensor (MRMS) quantitative precipitation estimation: Initial operating capabilities. *Bull. Amer. Meteor. Soc.*, **97**, 621–638, <https://doi.org/10.1175/BAMS-D-14-00174.1>.